*Journal of The Electrochemical Society*, 2022 **169** 044528

# Universal Correlation between Cathode Roughness Factor and $H_2$/Air Performance Losses in Voltage Cycling-Based Accelerated Stress Tests

**Roberta K. F. Della Bella,[=,*] Björn M. Stühmeier,[=,*,z] and Hubert A. Gasteiger[**]**

*Chair of Technical Electrochemistry, Department of Chemistry and Catalysis Research Center, Technical University of Munich, D-85748 Garching, Germany*

The loss of electrochemically active surface area (*ECSA*) in the cathode during load cycling remains a major durability issue for proton exchange membrane fuel cells (PEMFCs). Here, the degradation of low-loaded cathodes (0.1 $mg_{Pt}$ $cm^{-2}_{MEA}$) was investigated by accelerated stress tests (ASTs) in $H_2/N_2$ configuration, varying the upper potential limit (UPL, 0.85–1.0 V) and the hold time (1, 2, or 8 s) of the square wave voltage cycling profiles. A full voltage loss analysis was performed at beginning-of-life and after 100, 300, 1 k, 2 k, 5 k, 10 k, 20 k, 50 k, 100 k, 200 k, and 500 k cycles, determining: (i) the roughness factor (*rf*) via CO-stripping; (ii) the $H_2$-crossover; (iii) the cathode electrode's proton conduction resistance; (iv) the $H_2/O_2$ and $H_2$/air performance; and, (v) the $O_2$ transport resistance. It was found that the *ECSA*/*rf* deteriorates linearly vs the logarithm of the number of cycles or time at UPL, with higher slopes for harsher ASTs. The individual voltage losses were found to be either unaffected by the aging ($H_2$-crossover and proton conduction resistance) or depend exclusively on the cathode *rf* (mass/specific activity and $O_2$ transport resistances), independent of the AST procedure. This results in a universal correlation between $H_2$/air performance and *rf* during voltage cycling ASTs.

 [DOI: 10.1149/1945-7111/ac67b8]

Manuscript submitted February 9, 2022; revised manuscript received April 14, 2022. Published April 27, 2022.

The durability of the cathode catalyst layer remains a major challenge for the wide spread application of proton exchange membrane fuel cells (PEMFCs). The U.S. Department of Energy (DoE) set lifetime targets of at least 5,000 h for light-duty vehicles (LDV) and 30,000 h for heavy-duty vehicles (HDV) under drive cycle operation.[1] Hereby, many factors affect the durability of the membrane electrode assembly (MEA), namely cell reversal events that cause anode degradation, mechanical and chemical degradation of membrane and ionomer, corrosion of the carbon support of the cathode catalyst during start-up/shut-down or local hydrogen starvation events, and finally the loss of electrochemically active surface area (*ECSA*) of platinum in the cathode as a result of load cycling.[2–7] While many of these mechanisms can be mitigated to a significant degree by PEMFC system design, which has led to substantial improvements of PEMFC durability, the lifetime prediction based on accelerated stress tests (ASTs) remains challenging, particularly for the long lifetimes required for HDVs. In this study, we will therefore focus on the analysis of ASTs that mimic the Pt *ECSA* loss in the cathode electrode due to load cycling.

In order to simulate load cycling between relevant operation points, current research focuses on the development of appropriate voltage cycling (VC) based ASTs.[8–10] In general, load variations between low and high load, corresponding to high and low cathode potentials, respectively, cause repetitive surface oxidation and reduction of the Pt nanoparticles. This results in Pt dissolution and subsequent redeposition, which leads to a loss of electrochemically accessible platinum surface area due to both Pt nanoparticle growth via Ostwald ripening and platinum loss into the membrane phase that leads to the so-called Pt-band formation.[4,11,12] Due to their higher surface energies, the Pt dissolution/redeposition processes are more pronounced for smaller Pt nanoparticles, which therefore are more susceptible to Pt *ECSA* loss during load cycling.[4,12,13] Beside the effect of particle size, some studies highlight the importance of the interparticle distance for the various particle growth and migration phenomena, whereby an increase in interparticle distance (via, e.g., lowering the Pt loading on a given carbon support) enhances Pt dissolution phenomena, while a decrease in interparticle distance (via, e.g., increasing the Pt loading of the carbon support) will in contrast promote Pt nanoparticle agglomeration and coalescence.[14,15] It has further been shown that the overall loss of active Pt surface area is not homogenous across the thickness of the electrode: in the part of the electrode that is closest to the membrane, a depletion of Pt due to Pt loss into the membrane phase occurs, whereas in the part of the electrode that is closest to the gas diffusion layer (GDL), the platinum particle growth is the predominant cause of the Pt *ECSA* loss.[4] More recently, similar observations have also been made by Kneer et al.[16] The concomitant Pt *ECSA* loss during MEA aging by voltage cycling ASTs leads to severe $H_2$/air performance losses. At low current densities (<500 mA $cm^{-2}_{MEA}$), the induced voltage losses are mainly due to a loss in the activity of the platinum catalyst towards the oxygen reduction reaction (ORR), while in the middle and high current density region, additional $O_2$ mass transport resistances dominate the induced voltage losses. Here, the reduced roughness factor (*rf*), i.e., the reduced electrochemically active Pt surface area per geometric electrode area (in units of $cm^2_{Pt}$ $cm^{-2}_{MEA}$), implies that higher local $O_2$ and proton fluxes are required to sustain the ORR at a given geometric current density. These transport resistances, also known as Pt-specific or local $O_2$ mass transport resistances ($R_{O_2}^{local}$), have been reported to be especially pronounced for low-loaded cathodes, as they are predominantly inversely proportional to the *rf*.[17–19]

To evaluate the performance and *ECSA* losses during load cycle operation, the impact of different VC profiles on the degradation rate has been studied both in half-cell configuration with aqueous acidic electrolytes[2,20–22] and in membrane electrode assemblies (MEAs).[2,8,10,16,23,24] Despite the existence of standardized procedures, quantifying catalyst degradation with VC-based rotating disk electrode (RDE) experiments has proven challenging, as among 20 studies employing the same DoE protocol, the ORR mass activity retention was anywhere between 0 and 85% of the respective beginning-of-life (BoL) value.[22] Focusing on voltage cycling ASTs conducted in the PEM fuel cell environment, a variety of different voltage cycling profiles has been used in the literature, which complicates determining the reproducibility between different degradation studies. Still, when similar protocols are used with carbon supported Pt catalysts (Pt/C) with a comparable BoL *ECSA*, as it is the case in the studies of Stariha et al.[25] and Padgett et al.[23] for a ≈20 wt.% Pt catalyst supported on Vulcan carbon (Pt/V; TEC10V20E from Tanaka), or for analogous studies on Pt/C and

[=]Equal contribution.
[*]Electrochemical Society Student Member.
[**]Electrochemical Society Fellow.
[z]E-mail: bjoern.stuehmeier@tum.de

Pt-alloy/C catalysts with an *ECSA* of ≈45 $m^2 g_{Pt}^{-1}$,[26–28] the *ECSA* losses are reasonably comparable. Due to extensive research in recent years, the impact of gas composition (i.e., $H_2/N_2$ or $H_2$/air on anode/cathode), scan rate, hold time, temperature, relative humidity (*RH*), and the upper potential limit (UPL) on the *ECSA* degradation during VC-ASTs is well understood. Hereby, higher temperatures, high *RH*-values and high UPLs clearly accelerate *ECSA* loss, whereas the cathode gas composition does not affect the degradation rate.[8–10,16,24,29,30] Slower scan rates in case of triangular wave (TW, cyclic voltammetry based) profiles and longer hold times in case of square wave (SW, chronoamperometry based) profiles were shown to enhance the Pt *ECSA* loss per cycle but reduce the Pt *ECSA* loss per time, indicating that the number of cycles is a stronger stressor than the time at UPL.[8,31] Examining the impact of different voltage profiles, Harzer et al. found that mostly the UPL and the vertex hold times were responsible for the *ECSA* losses, whereby the degradation using a trapezoidal wave (TW-H, combination of linear scan and vertex holds) or a SW profile was essentially identical and much harsher compared to a TW profile.[10] In a similar study by Kneer et al., it was furthermore shown by asymmetric SW profiles that the hold time at UPL has a much more degrading effect than the hold time at the lower potential limit (LPL).[24] The role of the carbon support of the catalyst is an ongoing debate, whereby significant stability improvements for a porous carbon support have been shown in a study by Padgett et al.,[23] whereas Stariha et al.[25] did not find any significant differences between carbon supports. Finally, Ramaswamy et al.[27] showed that Pt particles originally placed within the nanopores of a porous carbon support become increasingly accessible upon voltage cycling.

While the mechanisms and accelerating factors for the Pt *ECSA* loss are well understood, only a small fraction of studies focusing on voltage cycling AST protocols additionally incorporate measurements for the determination of the various voltage loss terms during aging.[8,10,28] In fact, most of the published works concentrate on monitoring the *ECSA* by cyclic voltammetry (CV) or CO-stripping during the AST, while only comparing the air performance, catalyst activity and/or mass transport resistances at the end-of-life (EoL).[9,23,27–29,31] It is generally found that higher *ECSA* losses, i.e. harsher aging conditions, correlate with increased voltage losses from a reduced mass activity and increased oxygen mass transport resistances, while the specific activity increases due to particle growth.[8–10,23,27–29,31] However, in order to use voltage cycling ASTs for reliable lifetime predictions, a direct correlation of the Pt *ECSA* and the $H_2$/air performance losses for a given catalyst/MEA type, independent of the specific voltage cycling conditions, would be desired.

In this study, the development of the Pt *ECSA* and the individual voltage loss contributions was studied for 5 $cm^2$ MEAs with a commercial Pt/Vulcan catalyst using SW-based ASTs with different hold times and UPLs in order to find a suitable degradation model. For this, the *ECSA* was determined by CO-stripping, the ORR mass and specific activity were extracted from $H_2/O_2$ polarization curves, the $O_2$ mass transport resistances were calculated from limiting current measurements, and the proton conduction resistance in the cathode catalyst layer (CCL) was determined by electrochemical impedance spectroscopy (EIS). The development of these voltage losses is compared for all aging procedures at similar degrees of *rf*-losses. Based on the findings for the individual voltage loss contributions, a universal correlation between *rf* and the $H_2$/air performance of the cell will be shown. Finally, we will propose a new combined AST protocol for efficient lifetime prediction of VC-induced degradation based on the $H_2$/air performance targets.

## Experimental

Experimental details about the setup and measurement procedures can be found in previous publications,[10,32–35] but for reader's convenience, the most relevant information is summarized here.

***Fuel cell hardware and MEA preparation.—***All measurements were performed on a customized G60 test station (Greenlight Innovation Corp., USA) equipped with a potentiostat (Reference3000, Gamry, UK), using a 5 $cm^2$ active area single-cell hardware with graphite flow fields (7 parallel channels, one serpentine, 0.5 mm lands/channels; manufactured by Poco Graphite, Entegris GmbH, USA, according to our design[33]). Gas diffusion layers (GDLs, H14C10, Freudenberg KG, Germany) with a thickness of 170 ± 5 $\mu$m were compressed by 14 ± 1% by means of quasi-incompressible, PTFE-coated fiberglass gaskets (Fiberflon, Fiberflon GmbH & Co. KG, Germany). The cells were assembled at a torque of 12 Nm resulting in a GDL compression of ≈1.5 MPa on the active area (for details see Simon et al.[34]).

MEAs were prepared by the decal transfer method: The catalyst inks were prepared by mixing a commercial 19.8 wt.% Pt/V (TEC10V20E, Tanaka, Japan) catalyst, 1-propanol, and a water-based ionomer dispersion (700 EW, Asahi Kasei, Japan) in a 15 ml HDPE bottle containing 25.5 g of 5 mm $ZrO_2$ grinding balls. The carbon content of the dispersion was adjusted to 30 $mg_c$ $mL_{ink}^{-1}$ and the ionomer to carbon mass ratio (I/C) was set to 0.65 $g_I$ $g_C^{-1}$. The inks were mixed on a roller mill at 60 rpm for 18 h at 25 °C before being coated onto virgin PTFE foils with a 130 $\mu$m Mayer rod using an automated coater (K Control Coater, RK PrintCoat Instruments Ltd., England). Symmetrical MEAs were prepared by hot-pressing two 5 $cm^2$ decals at 155 °C for 3 min onto a 15 $\mu$m thick reinforced membrane (low EW, mitigated GORE-SELECT®, W. L. Gore & Associates GmbH, Germany). To minimize the deviation in the cathode loading between measurements, the electrodes were assigned to the cathode (0.103 ± 0.005 $mg_{Pt}$ $cm_{MEA}^{-2}$) and the anode electrode (0.10 ± 0.01 $mg_{Pt}$ $cm_{MEA}^{-2}$) after the respective loadings were determined. The thickness of the cathodes was ≈7.5 $\mu$m according to scanning electron microscopy (SEM) images of MEA cross-sections (see Fig. A·1).

***Voltage cycling procedure and MEA characterization measurements.—***The experimental testing procedure is summarized in the scheme shown in Fig. 1. The measurement procedure was optimized to minimize the amount of gas composition changes, unintended voltage cycles, and required $N_2$ purges. Unless otherwise specified, the cell was kept at 95% *RH* at all times to ensure operation close to full humidification, while avoiding flooding of the cell with liquid water. Furthermore, note that all pressures were measured and controlled at the inlet of the fuel cell and are stated as absolute pressures, and that potentials are given as cell potentials unless specified otherwise.

All MEAs were conditioned prior to testing by 8 cycles of the following voltage-controlled ramp-in procedure ($H_2$/air flow rates of 1390/3320 nccm (anode/cathode), 80 °C, 100% *RH,* and 150 $kPa_{abs}$): 0.6 V (45 min), open circuit voltage (OCV, 5 min), and 0.85 V (10 min).

Cathode CVs were recorded between 0.07–1.00 V vs the reversible hydrogen electrode reference potential ($V_{RHE}$, corrected by the Nernst shift of the counter electrode to a nominal hydrogen partial pressure of 100 kPa), using a scan rate of 150 mV $s^{-1}$ at 40 °C and 100 $kPa_{abs}$. During the measurement, the anode was fed with 200 nccm of fully humidified 5% $H_2$/Ar, while the cathode was flushed with a dry nitrogen flow of 200 nccm (reduced to 5 nccm while recording CVs).

In order to determine the proton conduction resistance in the cathode layer ($R_{H^+,cath}$ in units of Ω $cm_{MEA}^2$), three AC impedance spectra were recorded in blocking conditions (1000/1000 nccm $H_2/N_2$ flows at anode/cathode) at 80 °C, 95% *RH*, 270 $kPa_{abs}$, and at a potential of 0.2 V (peak-to-peak perturbation of 3.5 mV, 200 kHz to 0.2 Hz, 20 points per decade). The AC impedance response of the cathode electrode was then fitted to a transmission line model (using constant phase elements, ionic conduction resistances, and assuming negligible electrical resistances) in order to extract the proton

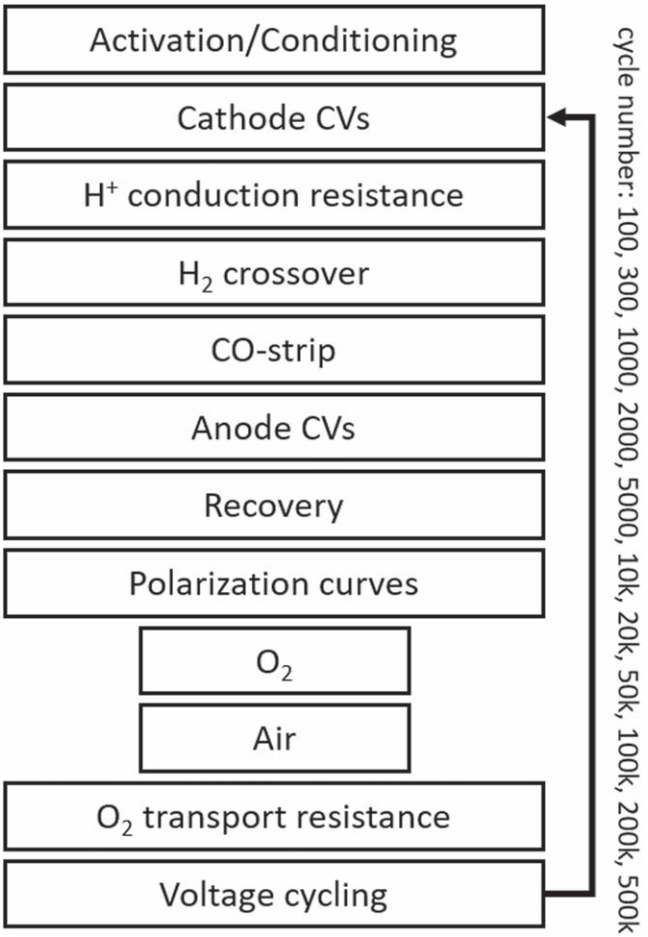


**Figure 1.** Scheme of the experimental procedure for the voltage cycling based MEA ASTs, whereby a full characterization was performed after each of the listed cycle numbers.

conduction resistance of the cathode electrode, $R_{H^+,\,cath}$ (for details see Liu et al.);[36–39] considering the cathode utilization, $R_{H^+,\,cath}$ was used to calculated the effective proton conduction resistance of the cathode electrode, $R^{eff}_{H^+,\,cath}$, from which the associated voltage losses can be determined.[40] The ohmic short of the membrane and the $H_2$-crossover were determined from measurements in $H_2/N_2$ (150/600 nccm) at 170 $kPa_{abs}$, 80 °C, and 95% *RH* by sequentially applying constant potentials of 0.3, 0.4, 0.5, 0.6 and 0.7 V for 2 min each.

CO-stripping measurements were performed by adsorbing CO (100 nccm flow of 10% CO in $N_2$) for 3 min at 40 °C and 150 $kPa_{abs}$, while holding a constant cathode potential of 0.1 $V_{RHE}$. After CO adsorption, the cell was purged with high purity $N_2$ (5.0) for ≈1 h to remove residual CO from the cell and the gas lines. A CV was recorded from the holding potential to 1.1 $V_{RHE}$ at a scan rate of 100 mV $s^{-1}$ to oxidize the adsorbed CO. Afterwards, two subsequent sweeps were recorded to ensure complete oxidation of CO from the catalyst surface. The area between the first anodic scan and its subsequent sweep was then used to determine the *rf*, using a specific charge of 420 $\mu C\ cm^{-2}_{Pt}$. For the CO-stripping measurements, the anode was purged with 5% $H_2$/Ar at 200 nccm.

After CO-stripping, anode CVs were recorded between 0.07–1.00 $V_{RHE}$ (anode potential) using a scan rate of 150 mV $s^{-1}$ at 40 °C and 100 $kPa_{abs}$. During the measurement, the anode was fed with a dry nitrogen flow of 200 nccm (reduced to 5 nccm while recording CVs), while the cathode was flushed with fully humidified 5% $H_2$/Ar at 200 nccm. This step was implemented to ensure that crossover CO, i.e., CO coming from the cathode side during the CO-stripping could not accumulate on the anode catalyst surface, where it would poison the hydrogen oxidation reaction (HOR) activity and might lead to increasing overpotentials over the course of aging.

Prior to each set of polarization curves (see scheme in Fig. 1), a MEA recovery step was introduced to recover reversible losses at the cathode electrode. It consisted of a hold in $H_2$/air (2000/5000 nccm) at 0.3 V for 2 h at 40 °C and 270 $kPa_{abs}$ under fully humidified conditions (100% *RH*). Afterwards, differential flow polarization curves in $H_2/O_2$ and $H_2$/air were carried out at 80 °C, 95% *RH* and 170 $kPa_{abs}$ with a flow rate of 2000/5000 nccm. The polarization curves were recorded in current controlled mode from low to high current densities up to 2.5 $A\ cm^{-2}_{MEA}$ To ensure reduction of Pt-oxides, the potential was held at 0.75 V for 15 min before each polarization curve. Stabilization of the resulting cell voltage was received by holding each current density point constant for 5 min and averaging the data points over the final 30 s. Afterwards, galvanostatic electrochemical impedance spectroscopy (GEIS) measurements were performed in the frequency range from 100 kHz to 10 Hz (amplitude adjusted to 10% of the applied current with a minimum of 20 mA $cm^{-2}_{MEA}$) to extract the high frequency resistance (*HFR*) from the *x*-axis intersect in the Nyquist plot. *HFR* and $R_{H^+,\,cath}$ (i.e., its effective contribution $R^{eff}_{H^+,\,cath}$) were used to correct the cell voltage in $H_2/O_2$ polarization curves for ohmic resistances and, additionally, the current density was corrected for the membrane short and $H_2$-crossover currents to obtain kinetic data (mass activity, specific activity, Tafel slope).

The total $O_2$ mass transport resistance ($R^{total}_{O_2}$) was obtained from limiting current measurements at 80 °C and 95% *RH* under differential flow conditions using 2000 nccm $H_2$ and 5000 nccm of $O_2/N_2$ mixtures on the anode and cathode, respectively. For each dry $O_2$ mole fraction of 2, 4, 7 and 11% $O_2$ in $N_2$, the cell potential was varied between 0.4 V and 0.05 V in steps of 0.05 V to determine the mass transport limited current densities (for details see Simon et al.[34]). To deconvolute $R^{total}_{O_2}$ into a pressure dependent ($R^{PD}_{O_2}$) and a pressure independent ($R^{PI}_{O_2}$) part according to Baker et al.,[41] limiting current measurements were conducted at 170, 270, and 400 $kPa_{abs}$.

Voltage cycling induced aging was performed at 80 °C, 95% *RH*, 100 $kPa_{abs}$, and $H_2/N_2$ flows of 200/75 nccm on anode/cathode. The SW voltage cycling ASTs were controlled by the Reference3000 potentiostat, whereby the potential step was completed in less than 0.1 s. The lower potential limit (LPL) was kept at 0.6 V, while the upper potential limit (UPL) was varied between 0.85 and 1.0 V, using hold times of 1, 2, or 8 s at each vertex potential. Here, the UPL of 1.0 V (at 8 s hold) was selected as comparison to the study of Harzer et al.,[10] while an UPL of 0.95 V resembles the open-circuit-voltage under $H_2$/air operation that was chosen as UPL in the studies by Kneer et al.[9,16,24] Finally, an UPL of 0.85 V was suggested by Ahluwalia et al. as a realistic value for load cycling in automotive applications.[42] The employed voltage cycling profiles and the end-of-life cycle numbers (EoL CN) are summarized in Table I. For each AST condition, two MEAs were prepared and evaluated; the measured MEA properties ($H_2$/air performance, ORR activities, etc.) are represented as average of these two measurements and the error bars represent the min/max values.

***Post-mortem MEA analysis.***—Scanning electron microscopy (SEM) images of ion-milled MEA cross-sections were taken for fresh as well as aged MEAs. In order to compare the cathode catalyst layer thickness before and after aging, the pristine MEA was subjected to the above mentioned conditioning step (confer Fig. 1) to ensure a more realistic comparability and to exclude any effects of cell assembly on the catalyst layer thickness. Prior to the ion-milling step, the GDL was peeled off and the 3-layer MEAs were fixated on adhesive Cu tape. Cross-sections were then prepared in an IB-19520 cryo cross-section polisher (JEOL Ltd., Japan) at −80 °C, using a multiple step polishing procedure with a first 3 h rough polishing (6.0 kV, 10/10 s on/off), followed by a 2 h fine polishing (4.0 kV,

**Table I. Characteristic parameters of the square wave (SW) profiles used for the voltage cycling based MEA ASTs that were performed at 100 $kPa_{abs}$, 80 °C, 95% RH, and $H_2/N_2$ flows of 200/75 nccm (anode/cathode). For all procedures, the lower potential limit (LPL) was kept constant at 0.6 V, while the upper potential limit (UPL), the hold time at each potential, and the end-of-life cycle number (EoL CN) were varied.**

| AST procedure | LPL [V] | UPL [V] | hold time [s] | EoL CN [#] |
|---|---|---|---|---|
| 1.00 V−8s | 0.6 | 1.0 | 8 | 10 k |
| 0.95 V−1s | 0.6 | 0.95 | 1 | 50 k |
| 0.85 V–8s | 0.6 | 0.85 | 8 | 50 k |
| 0.85 V−2s | 0.6 | 0.85 | 2 | 100 k |
| 0.85 V−1s | 0.6 | 0.85 | 1 | 500 k |

5/10 on/off). For thickness determination, SEM micrographs of the polished cross-sections were taken on a FE-SEM JSM 7500F (JEOL Ltd. Japan) in the secondary electron mode at 1 kV acceleration voltage and with a magnification of 2500× at 3 arbitrarily chosen locations for each cross-sectioned MEA. The thickness of the electrode was determined by integration of the electrode area with ImageJ (version 1.53 k) and dividing by the length of the image. In order to get more insights into the distribution of platinum across the MEA before and after voltage cycling based ASTs, SEM images were also taken in backscattering mode at 15 kV acceleration voltage and a magnification of 2500× at the same position as the ones used in the secondary electron mode.

## Results and Discussion

***ECSA determination.***—During voltage cycling based ASTs with Pt based catalysts, the *ECSA* is known to decrease substantially depending on the aging procedure. This effect can be seen exemplarily in Fig. 2a, which shows the cathode CVs of an MEA exposed to SW-aging between 0.6 and 1.0 V (see Table I). At BoL (black line), the characteristic Pt/C features of the hydrogen underpotential deposition ($H_{upd}$, region below 0.4 $V_{RHE}$) and of the Pt oxidation/reduction (starting above 0.75 $V_{RHE}$) are clearly visible. Over the course of cycling, the features decrease substantially due to a decrease in the cathode roughness factor (*rf*), resulting from the aforementioned Pt dissolution/redeposition mechanism. After 10,000 cycles between 0.6 and 1.0 V and with a hold time of 8 s (further on referred to as "1.00 V–8s"), the characteristic platinum features are no longer visible (orange line in Fig. 2a). Instead, the double layer capacity of the carbon support is observed, exhibiting the characteristic hydroquinone/quinone feature at ≈0.6 $V_{RHE}$.[43] The fact that this feature does not grow indicates that carbon corrosion does not play a significant role when using a SW cycling protocol up to 1.0 V, which agrees with the findings of Harzer et al.[10]

While the *ECSA* can be obtained from the $H_{upd}$ region, an increasing contribution of hydrogen evolution currents, that are mostly controlled thermodynamically at potentials near 0 $V_{RHE}$[44] and thus will not be affected by the aging induced degradation mechanism,[45] will lead to increasing errors in the quantification of the *ECSA* by $H_{upd}$ with decreasing cathode *rf* values.[46] Thus, CO-stripping is often used especially for the characterization of low-loaded or aged electrodes.[45,47] Representative CO-stripping voltammograms are given in Fig. 2b after subtraction of the second scan as baseline. As the second scan exhibits $H_{upd}$ features in the potential region below 0.4 $V_{RHE}$, the subtracted CO-stripping voltammograms would show negative currents in this region and thus, only data above 0.6 $V_{RHE}$ are shown. Similar to the $H_{upd}$ feature development, the CO oxidation peak decreases with increasing cycle number. The integration of the CO oxidation peaks is shown in Figs. 2c and 2d for the pristine and aged (10,000 cycles) cathode, respectively. When comparing the CO oxidation peak (see Fig. 2d) with the $H_{upd}$ features (orange line in Fig. 2a) for the same aged cathode, the advantage of the CO-stripping method becomes obvious: even for a catalyst exhibiting very low *rf* values that does not show distinguishable $H_{upd}$ features anymore, the CO oxidation peak is still distinct and clearly visible, which allows for a reliable *rf* determination. However, it was observed that the CO-stripping current, i.e., the difference between first and second scan, did not return to zero after the CO-strip but remained fairly constant at ≈0.2–0.3 mA $cm^{-2}_{MEA}$ (see Fig. 2d). This offset was observed in all cases and could also be reproduced for a pristine MEA without introducing CO, i.e., after the respective potential hold at 0.1 $V_{RHE}$ for 1 h in pure $N_2$ (5.0 purity), which means that it is most likely a partially irreversible oxidation of the carbon support rather than a CO oxidation current. While this offset does not have a significant effect on the *ECSA* determination at BoL (see Fig. 2c), the contribution of this current is significant after extended aging (see Fig. 2d). Therefore, the integration was conducted with a linear baseline between 0.6 and 1.0 $V_{RHE}$ even after having subtracted the subsequent scan as a first baseline (see gray areas in Figs. 2c and 2d).

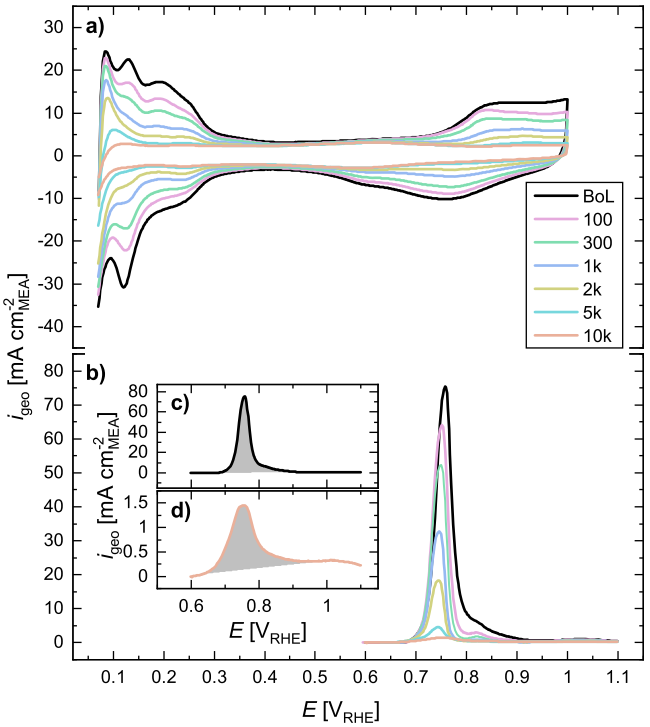


**Figure 2.** (a) CVs of the cathode after various cycles of aging during a SW based AST between 0.6 and 1.0 V with 8 s dwell time at each potential (further on referred to as 1.00 V–8s). CVs were measured at a scan rate of 150 mV $s^{-1}$ from 0.07 to 1.00 $V_{RHE}$ at ambient pressure and 40 °C under fully humidified conditions (see Experimental section). (b) Representative CO stripping voltammograms after subtraction of the subsequent anodic sweep for pristine and aged cathodes shown in the voltage range of 0.6-1.1 $V_{RHE}$ to exclude negative currents due to subtracted $H_{upd}$ features from the second scan. In addition, the zoomed in CO-stripping voltammograms are shown: (c) at BoL and (d) at EoL. CO-stripping voltammograms were recorded at 100 mV $s^{-1}$ up to 1.1 $V_{RHE}$ at 150 $kP_{abs}$, 40 °C, and 95% RH with 200 nccm 5% $H_2$/Ar and 5 nccm $N_2$ on anode and cathode, respectively. CO was adsorbed by introducing 10% $CO/N_2$ (100 nccm flow) for 3 min, followed by a $N_2$ purge for 1 h, while maintaining a constant cell potential of 0.1 $V_{RHE}$ at all times.

Since a reliable determination of the *ECSA* for cathodes with very low *rf* values by the $H_{upd}$ method is no longer possible and since CO-stripping generally yields slightly higher *ECSA*s than $H_{upd}$,[48] the *ECSA* results are solely determined by CO-stripping measurements throughout this study.

***ECSA development over the course of VC-ASTs.***—The development of the *ECSA* normalized to the initial BoL *ECSA* ($ECSA_{BoL}$)

for the different aging protocols (see Table I) vs the number of cycles (CN) or vs the time at the upper potential limit (UPL) is shown in Figs. 3a and 3b, respectively. As expected from previous studies, a higher UPL and longer hold times accelerate the *ECSA* loss per cycle (Fig. 3a), whereby the mildest aging protocol (0.85 V–1s, violet hexagon symbols) leads to the highest *ECSA* retention after 10,000 cycles, whereas the harshest aging protocol (1.00 V–8s, orange squares) shows the most pronounced decline in *ECSA,* reaching less than 5% of the initial *ECSA* after 10,000 cycles. When comparing the degradation after 10,000 cycles to other studies by Stariha et al.[25] and Padgett et al.[23] that used the same ≈20 wt.% Pt/V catalyst and an UPL of 0.95 V, their *ECSA* loss of ≈50% and ≈65%, respectively, was slightly lower than the *ECSA* loss of ≈75% found in our study (red triangle at 10,000 cycles in Fig. 3a). These discrepancies are most likely the result of slightly different protocols and setups. A degradation caused by the excessive characterization procedure in this study can be excluded on the basis of reference measurements that yielded the exact same *ECSA* after 10,000 cycles when the extensive MEA characterization steps were only performed at BoL and after 10,000 cycles (data not shown).

Interestingly, very similar values of 82 ± 2% normalized *ECSA* were observed after a settle-in phase in the first 100 cycles for all aging procedures with an UPL below 1 V (see Table II); only the harshest procedure with an UPL of 1.00 V and a hold time of 8 s showed a significantly lower normalized *ECSA* of 74 ± 1% after 100 cycles. An initial *ECSA* decay independent on the used aging condition has already been observed by Harzer et al., although they did not explicitly comment on it.[10] However, for the same Pt/V catalyst that is used here, they showed that the pristine Pt/V catalyst contained a significant fraction of sub-1.5 nm diameter Pt particles. Thus, when considering the reported particle size effects,[12,49,50] it seems likely that these smallest Pt particles would be sufficiently instable, so that within the first 100 cycles they are likely to dissolve even under relatively mild cycling conditions, leading to the here observed initial *ECSA* losses.

Another universal behavior is the linear *ECSA* decay after 100 cycles in all cases when plotting the normalized *ECSA* (i.e., $ECSA/ECSA_{BoL}$) against the logarithm of the cycle number (CN), a behavior which has already been observed previously.[13] This linearity differs strongly from the 1st order decay rate that was found in earlier studies by Debe et al.[51] and Bi et al.[52,53] for VC-ASTs with an UPL of 1.2 $V_{RHE}$ and resulted in a linear behavior when plotting the logarithm of the normalized *ECSA* against the CN. Based on these works, Kneer and Wagner proposed a modified 1st order kinetic rate model for VC-ASTs with lower UPLs but in most cases, the model underestimated the *ECSA* loss up to ≈50% of the BoL *ECSA* and overestimated the *ECSA* loss thereafter,[9] thus indicating that the model does not accurately describe the *ECSA* degradation at limited UPLs (⩽1.0 $V_{RHE}$). The most likely explanation of these different *ECSA* loss behaviors is the different origins of the Pt *ECSA* losses with carbon corrosion and Pt detachment/migration/coalescence being the dominating degradation mechanisms when using an UPL of 1.2 $V_{RHE}$, whereas Pt dissolution/redeposition dominates at limited UPLs (⩽1.0 $V_{RHE}$).[4,6,13] Only below a normalized *ECSA* of ≈12.5% (horizontal red dashed line in Fig. 3) that corresponds to a *rf* of ≈10 $cm^2_{Pt}\,cm^{-2}_{MEA}$ (the reasoning for this specific value will be discussed in detail later), a deviation from the linear behavior is observed. This apparent stabilization of very small *ECSA* values after extended cycling has been discussed to be due to a thermodynamic stabilization of larger Pt particles.[10] This observed linear trend can be used to determine a phenomenological normalized *ECSA*-loss rate constant ($k_{ECSA\text{-loss}}$) that is an empirical measure of

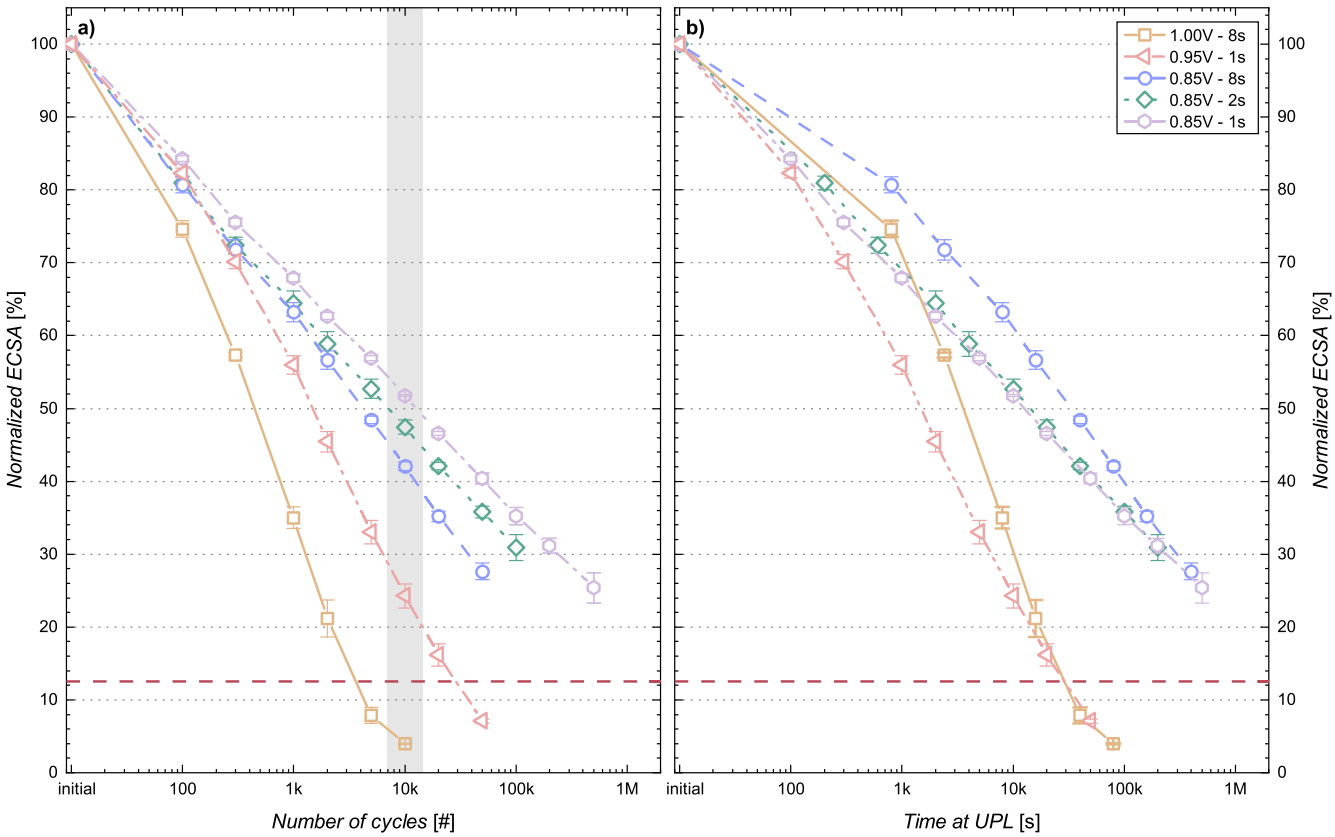


**Figure 3.** Loss of normalized cathode ECSA (i.e., $ECSA/ECSA_{BoL}$) plotted either vs: (a) the number of cycles, or (b) the time at the upper potential limit (UPL). The initial BoL value of the ECSA for all cathodes is $ECSA_{BoL} = 75.2 \pm 0.6\ m^2\ g^{-1}_{Pt}$, corresponding to rf values of 79.0 ± 4.4 $cm^2_{Pt}\,cm^{-2}_{MEA}$ at Pt cathode loadings of 0.103 ± 0.005 $mg_{Pt}\,cm^{-2}_{MEA}$. The horizontal red dashed line at 12.5% normalized ECSA (corresponding to a rf of ≈10 $cm^2_{Pt}\,cm^{-2}_{MEA}$) marks the lower limit that was used for the linear fits the normalized ECSA vs. the logarithm of the cycle number (see Eq. 1 and Table II). The gray shaded area marks the ECSA values after 10,000 cycles.

**Table II. Least-squares regression parameters for the relationship between the normalized ECSA ($ECSA/ECSA_{BoL}$) and the logarithm of the number of cycles (see Eq. 1) for the different voltage cycling ASTs shown in Fig. 3a. The normalized ECSA data were fitted between their normalized value at 100 cycles ($ECSA_{100CN}/ECSA_{BoL}$) and all the measured $ECSA/ECSA_{BoL}$ values that were higher than 12.5% (i.e., above the horizontal red dashed line in Fig. 3a). The resulting parameter fits of the $ECSA_{100CN}/ECSA_{BoL}$ values and of the slopes ($k_{ECSA-loss}$) are given below.**

| UPL of the VC-AST | 1.0 V | 0.95 V | 0.85 V | | |
|---|---|---|---|---|---|
| hold time at UPL | 8 s | 1 s | 8 s | 2 s | 1 s |
| $ECSA_{100CN}/ECSA_{BoL}$ [%] | 74.6 ± 1.2 | 82.3 ± 0.7 | 80.7 ± 1.1 | 80.9 ± 1.0 | 84.3 ± 0.4 |
| $k_{ECSA\text{-}loss}$ [% $dec^{-1}$] | 40.3 ± 2.3 | 28.8 ± 0.5 | 19.9 ± 0.4 | 16.7 ± 0.1 | 16.2 ± 0.1 |

how harsh an aging protocol is (Eq. 1).

$$ECSA/ECSA_{BoL} = ECSA_{100CN}/ECSA_{BoL} - k_{ECSA\text{-}loss} \cdot \log(CN) \quad [1]$$

For the *ECSA* data obtained from the different AST protocols shown in Fig. 3a, the $k_{ECSA\text{-}loss}$ values obtained from linear regression fits of the normalized *ECSA* data obtained between 100 cycles ($ECSA_{100CN}/ECSA_{BoL}$) and the number of cycles up to which the normalized *ECSA* values remain above 12.5% are given in Table II. The slopes gradually increase with longer hold times from 1 to 8 s and with higher UPLs from 0.85 to 1.0 V, thereby confirming the Pt *ECSA* trends that were observed in previous voltage cycling studies.[8–10]

The assumption that Pt dissolution/redeposition is the dominating aging mechanism for voltage cycling ASTs with an UPL of $\leqslant$1.0 $V_{RHE}$ is confirmed by post-mortem analysis of MEA cross-sections via scanning electron microscopy (SEM) in backscattered mode (see Fig. 4). While Pt is distributed homogeneously throughout the cathode catalyst layer at BoL (see Fig. 4a), a pronounced anisotropy of the Pt distribution across the cathode catalyst layer (depicted on top of the images in Fig. 4) is observed after voltage-cycling. For the severely degraded cathode after 10,000 cycles of the 1.00 V–8s AST protocol (see Fig. 4b), a pronounced Pt band can be seen at the membrane-electrode interface, whereas the electrode is completely depleted of Pt close to the membrane. According to Zhang et al.,[54] the position of the Pt band is governed by the partial pressures of $H_2$ and $O_2$ in anode and cathode compartment, respectively, and since the $O_2$ partial pressure is 0 kPa during voltage cycling in $H_2/N_2$ configuration, the Pt band position is expected to be directly at the electrode-membrane interface. According to Ferreira et al.,[4] the observed depletion of Pt adjacent to the membrane with Pt being maintained next to the GDL is a clear indication for a dominating Pt dissolution/redeposition mechanism. On the other hand, others reported that Pt coalescence would contribute to the overall *ECSA* losses even when the UPL is limited to $\leqslant$1.0 $V_{RHE}$.[23] While we believe that the latter mechanism might be a significant factor in the Pt particle growth-dominated region (close to the cathode/GDL interface), the origin of the Pt depletion next to the membrane must be caused by Pt dissolution and loss into the membrane phase. For the less severe aging protocols with an UPL of 0.85 $V_{RHE}$ and hold times of 8 s (Fig. 4c) or 1 s (Fig. 4d), a similar but less pronounced trend of Pt band formation and Pt depletion adjacent to the membrane is observed at EoL, in accordance with the less severe *ECSA* degradation at EoL for these protocols. Within the measurement accuracy, the initial cathode catalyst layer thickness was maintained after the ASTs (see Table III), which confirms that carbon corrosion did not contribute significantly to the cathode degradation.

As mentioned previously, the hold time at the UPL has been reported to affect the degradation differently, depending on whether it is looked at as a function of CN or the time at UPL ($t_{UPL}$). In Fig. 3b, the normalized *ECSA* is shown over the logarithm of the time at UPL, whereby the time at UPL is the product of CN and hold time ($t_{hold}$). Due to the nature of the logarithmic scale, this results in a right-shift of all data points by the factor $\log(t_{hold})$ and the $k_{ECSA\text{-}loss}$ values representing the slope in % $dec^{-1}$ (Table II) remain the same (Eq. 2).

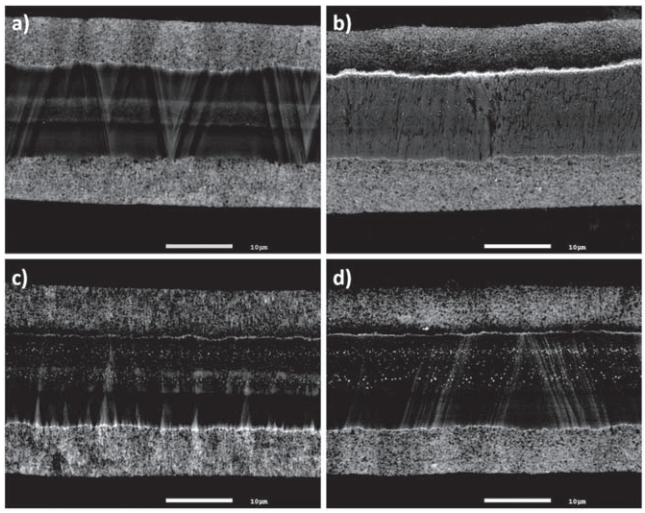


**Figure 4.** Post mortem SEM cross-section images of MEAs after (a) BoL characterization as well as after voltage cycling ASTs using the (b) 1.00 V–8s, (c) 0.85 V–8s, or (d) 0.85 V–1s protocols. Images were taken by SEM at a magnification of 2500× in electron back-scattering mode. The cathode catalyst layer of the MEA is shown in each image at the top; the white scale bar at the bottom of each image represents 10 $\mu$m.

$$\log(t_{UPL}) = \log(t_{hold} \cdot CN) = \log(t_{hold}) + \log(CN) \quad [2]$$

Still, this representation allows for some interesting conclusions. First, the normalized *ECSA* of the harshest protocol (1.00 V–8s, orange squares in Fig. 3b) is higher than that for the fast cycling to a lower potential of 0.95 V (0.95 V–1s, red triangles) in the whole linear region, which indicates that for a given $t_{UPL}$ value, a few long OCV periods are less detrimental than many short high/low-load cycles. The same holds true when the UPL is the same, as can be seen for the AST data with UPL = 0.85 V: for the same $t_{UPL}$ value, a few cycles with long hold times (8 s, blue circles) induce significantly lower *ECSA* loss compared to more cycles with shorter hold times of 2 s (green diamonds) or 1 s (pink hexagons). This indicates that the number of cycles is a stronger trigger for degradation than the total time at UPL. However, due to the higher slope for longer hold periods, there is a crossover point at which the *ECSA* degradation is the same for different hold times. In this case, the crossover point occurred after ≈500,000 cycles with ≈25% *ECSA* remaining, i.e., at a point that would be considered past EoL.

The effect of the hold time at the same UPL can be examined by the data taken for the same UPL of 0.85 V but for different hold times (see Fig. 3b). Assuming that the anodic and the cathodic potential steps lead to a transient dissolution of platinum, as suggested by rotating ring disk electrode measurements[55,56] and by online mass spectrometry,[57] one would expect that the $t_{hold}$-averaged amount of dissolved platinum would decrease with increasing $t_{hold}$, so that the *ECSA* loss vs $t_{hold}$ should decrease with increasing time at

**Table III. Averaged cathode catalyst layer thicknesses for MEAs after conditioning (BoL) or after a given number of AST cycles (CN) with different UPLs values (0.85 V or 1.00 V) and hold times (1 or 8 s). These ASTs represent the most harsh (1.00 V–8s) and least harsh aging protocols (0.85 V–8/1s) and the MEAs from these ASTs were therefore chosen for further investigation using SEM imaging. The averaged cathode electrode thickness values were calculated by dividing the integrated electrode area by the length of the SEM cross-section images taken in the secondary electron mode (confer Fig. A·1); the error bars represent the standard deviation of the thus obtained thicknesses from at least three images taken at arbitrarily chosen positions on the same cross-sectioned MEA.**

| MEA history | CN [#] | Cathode thickness [$\mu$m] |
|---|---|---|
| BoL | 0 | 7.2 ± 0.5 |
| 1.00 V−8s AST | 10 k | 7.5 ± 0.3 |
| 0.85 V−8s AST | 50 k | 7.5 ± 0.4 |
| 0.85 V−1s AST | 500 k | 7.2 ± 0.4 |

UPL. This would explain why the *ECSA* loss vs time at UPL is lower for the 0.85 V–8s compared to the 0.85 V–2s AST (see Fig. 3b). It is inconsistent, however, with the observation that the *ECSA* loss vs time at UPL is essentially identical for the 0.85 V–2s and the 0.85 V–1s AST data (see Fig. 3b). One possible explanation might be that at very short hold times the typically significant platinum loss into the membrane/ionomer phase during voltage cycling[4,52] is reduced due to an insufficient mobility of dissolved platinum ions in the ionomer phase, thereby reducing the platinum loss into the membrane/ionomer phase per cycle. Whether this is the case could be determined by estimating the diffusion length ($x$) of dissolved platinum ions in the ionomer phase of the cathode electrode over the hold time (via $x \approx (D_{\mathrm{Pt,\ eff}} \cdot t_{\mathrm{hold}})^{0.5}$), but this requires that the effective diffusion coefficient of platinum ions in the membrane/ionomer phase ($D_{\mathrm{Pt,\ eff}}$) be known. Unfortunately, the $D_{\mathrm{Pt,\ eff}}$ values in the ionomer phase of the catalyst layer that are used in voltage cycling models vary widely (from $1{\cdot}10^{-6}$ cm$^2$ s$^{-1}$[58] to $1.5{\cdot}10^{-9}$ cm$^2$ s$^{-1}$[53]), and to our knowledge only two actual measurements exist for the platinum diffusion coefficient in Nafion® membranes ($D_{\mathrm{Pt}}$) at 25 °C: $\approx 4{\cdot}10^{-7}$ cm$^2$ s$^{-1}$[59](determined by online mass spectrometry) and $\approx 1.4{\cdot}10^{-8}$ cm$^2$ s$^{-1}$ (measured for $(PtCl_6)^{2-}$ ions[60]). In order to obtain the $D_{\mathrm{Pt,\ eff}}$ values in the ionomer phase of the catalyst layer at 80 °C, these $D_{\mathrm{Pt}}$ values must be multiplied by the typical ionomer volume fraction in the electrode ($\varepsilon_{\mathrm{ionomer}} \approx 0.2$[4]) and the ≈5-fold increase for ionic diffusion coefficients in a Nafion® membrane between 25 and 80 °C (measured for $Co^{2+}$ and $Ce^{3+}$[61]). Coincidentally, both corrections cancel each other, so that the measured membrane $D_{\mathrm{Pt}}$ values at 25 °C and the estimated $D_{\mathrm{Pt,\ eff}}$ values in the catalyst layer at 80 °C turn out to be numerically identical, i.e., $D_{\mathrm{Pt,\ eff}} \approx (1.4\text{–}40){\cdot}10^{-8}$ cm$^2$ s$^{-1}$. For this range, the $x$ values for $t_{\mathrm{hold}} = 1$ s would range between ≈1.2–6 $\mu$m, which is less than the cathode electrode thickness (≈7.5 $\mu$m, see Table III), making it plausible that the loss of platinum into the membrane/ionomer phase per cycle could be reduced for such short hold times, which in turn could explain the observed reduced *ECSA* losses per cycle and the similar *ECSA* losses per time at UPL for very short $t_{\mathrm{hold}}$ values. According to the post mortem analysis of cross-sectioned MEAs by SEM, the fraction of Pt lost into the membrane/ionomer phase and the depletion of platinum in the cathode electrode in the vicinity of the membrane (appearing as dark region in in Figs. 4c and 4d) seems to be essentially the same for hold times of 8 and 1 s, indicating that the hold time does not significantly affect the degradation mechanism when comparing two MEAs with similar remaining *ECSA* values.

Finally, it should be noted that most studies take the *ECSA* loss during voltage cycling ASTs as primary parameter to describe the aging of the cathode electrode and the associated fuel performance degradation. In order to allow for an easier comparison with the literature, this convention has been adopted in the preceding section as well. Here, the *ECSA* is generally obtained by quantifying the cathode roughness factor (in $\mathrm{cm}^2_{\mathrm{Pt}}\,\mathrm{cm}^{-2}_{\mathrm{MEA}}$), namely by $H_{\mathrm{upd}}$ or CO-stripping measurements that are then normalized by the initial Pt loading of the cathode electrode (in $\mathrm{mg}_{\mathrm{Pt}}\,\mathrm{cm}^{-2}_{\mathrm{MEA}}$). Here, the term "*ECSA*," i.e., the mass normalized Pt surface area of a catalyst, is usually associated with specific property of a catalyst, reflecting its platinum particle size distribution. However, as voltage cycling progresses, platinum in the cathode electrode is increasingly lost into the membrane/ionomer phase[4,52] (illustrated, e.g., by the Pt-band formation in the membrane, see Fig. 4b), resulting both in a loss of platinum from the electrode into the membrane/ionomer phase and in a variation of the platinum concentration (see Fig. 4) and the Pt particle size across the cathode electrode thickness,[4] so that the nominally calculated "*ECSA*" does not anymore represent a catalyst-specific property, i.e., an *ECSA* of 50 m$^2$ $g_{\mathrm{Pt}}^{-1}$ after aging describes a completely different situation with regards to the platinum catalyst than the same *ECSA* value for a pristine catalyst taken at BoL. In contrast, the *rf* value (i.e., the active Pt area per geometric area) is associated with the properties of the catalyst layer rather than the catalyst that comprises the catalyst layer, and thus remains an accurate representation of the state of the MEA (i.e., represents a direct measurement). Since the *rf* avoids the false impression of an underlying average particle size that would be associated with the *ECSA*, the *rf* will be used as the main state-of-health descriptor in the following parts of our study.

***Qualitative assessment of voltage losses in $H_2$/air polarization curves.***—$H_2$/air polarization curves of pristine and aged catalysts after 10,000 cycles are shown in Fig. 5. As expected, more severely degraded MEAs, i.,,e, MEAs with larger normalized *ECSA* losses (see gray area in Fig. 3a for reference), showed higher performance losses compared to the BoL performance (black squares). An exception to this trend is the essentially identical performance of the MEAs subjected to the 0.85 V–8s AST (blue circles) and to the 0.85 V–2s AST (green diamonds). This, unfortunately, is the result of a slightly below average BoL performance of the MEAs that had been used for the 0.85 V–2 s measurement series (≈25 mV at the highest current density; confer right-most green diamonds in Fig. 12), resulting in a $H_2$/air performance after 10,000 cycles that is the same as that of the MEAs subjected to the harsher 0.85 V–8s AST that experienced a higher *ECSA* loss. The most severe differences can be observed in the high current density region, where increasing oxygen mass transport overpotentials directly correlate with the decrease in the normalized *ECSA* (see Fig. 3a) and thus the roughness factor. For the most degraded catalyst with a *rf* of only ≈3 $\mathrm{cm}^2_{\mathrm{Pt}}\,\mathrm{cm}^{-2}_{\mathrm{MEA}}$ (1.00 V–8s, orange squares in Fig. 5), this results in a maximum current density of only 500 mA $\mathrm{cm}^{-2}_{\mathrm{MEA}}$ before the cell potential goes below the specified cutoff of 0.2 V. In contrast to the mass transport penalties at low *rf* values, ORR kinetic overpotentials should have a minor contribution to the overall voltage losses due to the logarithmic nature of the Tafel kinetics, where a 90% *rf*-loss is required for an overpotential increase by ≈70 mV.[62,63] Indeed, for an *ECSA* or *rf* loss of ≈53% (0.85 V–2s, green diamonds), the potential at 500 mA $\mathrm{cm}^{-2}_{\mathrm{MEA}}$ decreased by less than 10 mV, which is less than the ≈20 mV one would expect based on simple Tafel kinetics with a constant exchange current density, and thus already hints at an increase of the ORR specific activity that has been observed in previous studies.[10,23,64]

For all MEAs, *HFR* values of 26–33 mΩ $\mathrm{cm}^{-2}_{\mathrm{MEA}}$ were obtained at BoL and stayed constant for an individual MEA over aging (Fig. 5b). Similarly, the $H_2$-crossover current density stayed constant at ≈5–6 mA $\mathrm{cm}^{-2}_{\mathrm{MEA}}$ for all MEAs during aging, except for a decrease to ≈2–3 mA $\mathrm{cm}^{-2}_{\mathrm{MEA}}$ at extremely low *rf* values ($<10$ $\mathrm{cm}^2_{\mathrm{Pt}}\,\mathrm{cm}^{-2}_{\mathrm{MEA}}$). The origin of this decrease is unknown as measurements in $H_2/N_2$ configuration cannot replicate the $H_2$–$O_2$ recombination effect of a Pt-band in the membrane that might cause

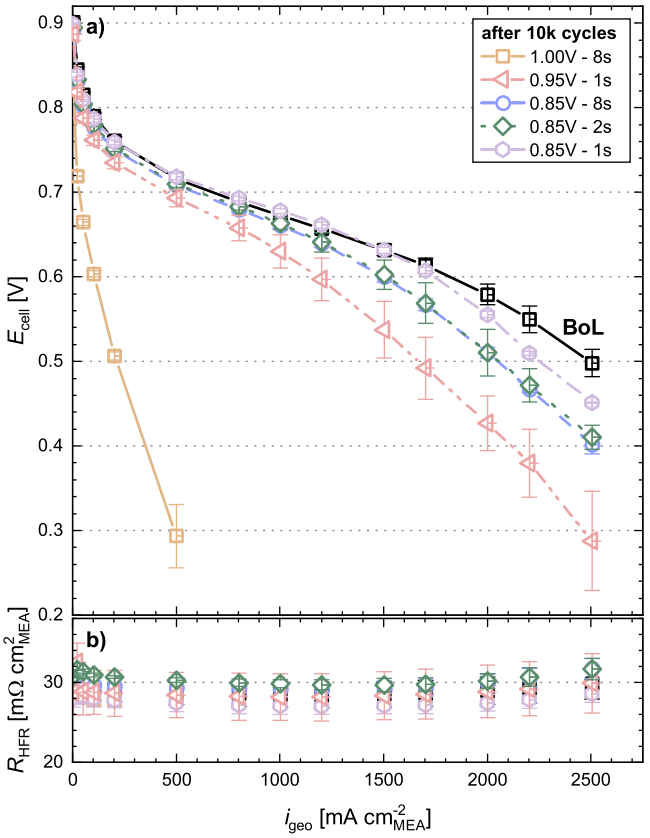


**Figure 5.** (a) Differential flow $H_2$/air (2000/5000 nccm) polarization curves at 170 $kPa_{abs}$, 80 °C, and 95% RH of MEAs with 0.103 ± 0.05 $mg_{Pt}$ $cm^{-2}_{MEA}$ cathode loadings at BoL (black symbols) and after 10,000 aging cycles (for respective ECSA losses see gray highlighted area in Fig. 3a); (b) corresponding high frequency resistance (HFR) values. After 10,000 cycles, the error bars represent the mean absolute deviation of two independent measurements, while the BoL data are averaged over all 10 MEAs and error bars represent the standard deviation.

a reduced $H_2$-crossover during $H_2$/air operation and the HOR activity of the cathode should be sufficiently high for $H_2$-crossover measurements even at these low *rf* values.[47] Considering the constant *HFR* values and the very low $H_2$-crossover currents, a significant degradation of the membrane over the course of the ASTs can be excluded.

Finally, the proton conduction resistance of the cathode electrode ($R_{H^+,cath}$) remained rather constant for the MEAs subjected to different aging protocols over the course of aging (≈20–25 mΩ $cm^2_{MEA}$; see Fig. 6), i.e., did not vary significantly despite the large changes in *ECSA* or *rf* (see Fig. 3). Therefore, ionomer degradation induced changes in the proton conduction pathway that have been shown to result in reversible and irreversible voltage losses after dry operation can be excluded as a major voltage loss contribution.[65]

Overall, ohmic resistances were found to be unaffected by aging, which leaves changes in the catalytic activity and increasing mass transport resistances as the main causes for the deteriorating $H_2$/air performance. Both aspects will be discussed in detail below.

***Dependence of the ORR activity losses on cathode rf.***—To evaluate the cathode activity, $H_2/O_2$ polarization curves were recorded under differential flow conditions. The Tafel plots of the *HFR*- and $R_{H^+,cath}$-corrected voltage against the logarithm of the specific current density that was corrected by the $H_2$-crossover ($i_{H2\text{-}cross}$) and the ohmic short current ($i_{short}$) are shown in Fig. 7 for the pristine and for the most severely degraded MEAs of each AST protocol with a final *rf* >10 $cm^2_{Pt}$ $cm^{-2}_{MEA}$ (Fig. 7a) or with a final *rf*

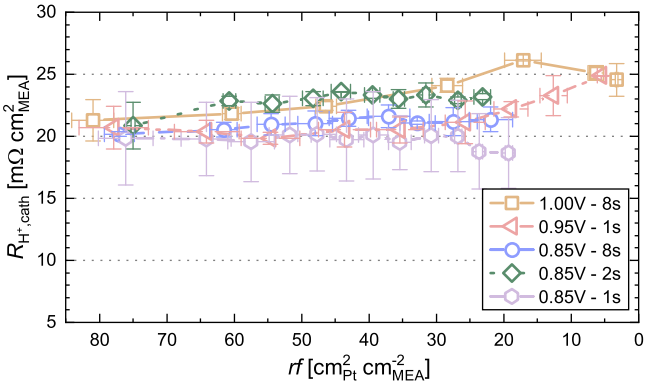


**Figure 6.** Variation of the proton conduction resistance ($R_{H^+,cath}$) of the cathode electrode as a function of rf over the course of the various voltage cycling ASTs (see Table I), determined from transition line model fits of AC impedance spectra that were recorded in $H_2/N_2$ (150/600 nccm) configuration at 270 $kPa_{abs}$, 80 °C, and 95% RH. Error bars represent the mean absolute deviation between two independent measurements.

<10 $cm^2_{Pt}$ $cm^{-2}_{MEA}$ (Fig. 7b). This distinction is made based on the empirically found linear relationship between the normalized *ECSA* (or the *rf*) and the logarithm of the cycle number that holds until the *rf* decreases to below ≈10 $cm^2_{Pt}$ $cm^{-2}_{MEA}$ (see horizontal red dashed line in Fig. 3a); this limit seems to mark a change in the degradation behavior and, furthermore, below this limit a characterization of the MEA with regard to specific surface area (see Fig. 2) and limiting current measurements (shown later in Fig. 9) becomes challenging and error prone.

Overall, a similar development can be seen for all cycling procedures when comparing the Tafel plots at BoL (black squares, averaged over all MEAs) to that of the aged MEAs (procedure and respective CN given in the legend of Fig. 7a). As long as the *rf* remains above 10 $cm^2_{Pt}$ $cm^{-2}_{MEA}$ (Fig. 7a), a constant Tafel slope of 75 ± 3 mV $dec^{-1}$ was found, similar to previously reported values for the same catalyst and setup;[10,66] it is slightly higher than the 70 mV $dec^{-1}$ that correspond to a cathodic transfer coefficient of $\alpha_c = 1$ for the ORR (gray line for reference) and that has often been assumed for carbon supported Pt catalysts.[63,67] Over the course of aging, the Tafel curves gradually shift towards higher potentials (only the (near-)EoL curves are depicted for clarity), indicating an increase in specific activity with decreasing *rf*, i.e., with increasing Pt particle size. However, at current densities higher than ≈0.1 *A* $cm^{-2}_{Pt}$ (only reached for *rf* < 25 $cm^2_{Pt}$ $cm^{-2}_{MEA}$ for the maximum current density of 2.5 *A* $cm^{-2}_{MEA}$), the curves start to deviate from the initial Tafel slope, leading to additional overpotentials. Similar deviations from the expected Tafel kinetics at low *rf* values have been reported by other researchers for pristine[68,69] and aged electrodes[10] alike. The origin of these losses at high specific current densities are still debated, but the proposed causes include a limited dissolution of oxygen into the ionomer phase, an intrinsically high transport resistance of the thin ionomer phase covering the Pt nanoparticles, a limited effective ionomer surface, or a decrease of the ORR kinetics at low cathode potentials.[19,48,70–74]

An even more pronounced deviation from the ≈70 mV $dec^{-1}$ Tafel slope is observed for aged MEAs with ultra-low *rf* values of < 10 $cm^2_{Pt}$ $cm^{-2}_{MEA}$ (Fig. 7b). Already in the low specific current density range, i.e., up to 0.03 *A* $cm^{-2}_{Pt}$, a much higher Tafel slope of ≈120 mV $dec^{-1}$ was found. This apparent increase in Tafel slope has previously been ascribed to a shift in the rate determining step of the ORR, leading to an increase in Tafel slope from 70 mV $dec^{-1}$ ($\alpha_c = 1$) to 140 mV $dec^{-1}$ ($\alpha_c = 0.5$).[74,75] However, this increase had been hypothesized to be due to a potential dependent change in the surface coverage of Pt with oxygen-containing species,[74,75] which clearly cannot explain the higher Tafel slopes at potentials

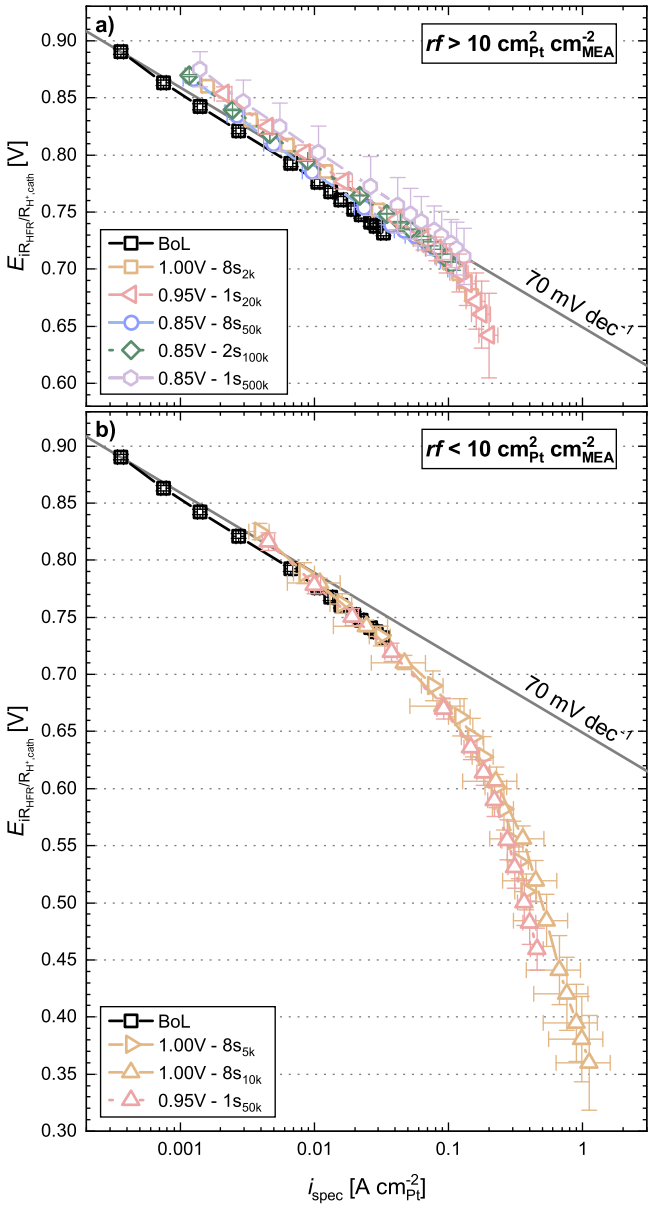


**Figure 7.** Tafel plot representation of HFR- and $R_{H^+,\,cath}$-corrected potential vs specific current density of differential flow $H_2/O_2$ (2000/5000 nccm) polarization curves at 170 $kPa_{abs}$, 80 °C, and 95% RH after different ASTs (in the figure, the respective cycle numbers are given as indices for each AST protocol). (a) Aged cathodes with rf >10 $cm^2_{Pt}\,cm^{-2}_{MEA}$ (corresponding to either the $H_2$/air performance at EoL or near EoL, i.e., above the horizontal red dashed line in Fig. 3); (b) aged cathodes with rf <10 $cm^2_{Pt}\,cm^{-2}_{MEA}$ (corresponding to three data sets below the horizontal red dashed line in Fig. 3). Error bars represent the mean absolute deviation between two independent measurements (aged electrodes), or the standard deviation of all MEAs (BoL). The black solid line with a slope of 70 mV $dec^{-1}$ that very closely describes the BoL performance serves as a guide-to-the-eye. Error bars represent the mean absolute deviation between two independent measurements.

above 0.75 V (i.e., between 0.005-0.030 $A\,cm^{-2}_{Pt}$ in Fig. 7b). It has also been suggested that higher Tafel slopes might be the result of additional local proton conduction resistances in the vicinity of the Pt nanoparticles, which would not be captured by through-plane proton conduction resistance measurements (i.e., by the thus determined $R_{H^+,\,cath}$ value).[76] While a ≈50 mV $dec^{-1}$ increase in Tafel slope (i.e., from ≈70 to ≈120 mV $dec^{-1}$) is quite severe, it should be noted that in a Pt dissolution/redeposition degradation mechanism, where reversible Pt dissolution/redeposition concurs with irreversible Pt loss into the membrane, it may be possible that the last remaining large Pt particles in the cathode electrode (at extremely low *rf*) could be poorly contacted by the proton conducting ionomer, which would also lead to an additional voltage loss that is not captured by the commonly used diagnostics.

For all electrodes shown in Fig. 7, very large deviations from the ≈70 mV $dec^{-1}$ Tafel slope are observed at specific current densities above ≈0.10 $A\,cm^{-2}_{Pt}$ (Fig. 7a) or already above ≈0.03 $A\,cm^{-2}_{Pt}$ in case of very low roughness factors (Fig. 7b), with apparent Tafel slopes of several hundreds of mV $dec^{-1}$. This cannot be explained by a change in the reaction mechanism alone anymore, and is most likely the result of a Pt-specific oxygen mass transport resistance. Although oxygen mass transport in the gas phase can be neglected for the here shown measurements with pure $O_2$, additional local $O_2$ transport resistances at the Pt/ionomer interface have widely been reported in the literature.[17,19,48,71] These local $O_2$ transport resistances that are inversely proportional to the *rf* value will be discussed in detail in the next section.

To determine the kinetic ORR activity, a linear regression performed in the current range between 50–500 mA $cm^{-2}_{MEA}$ for *rf* values >10 $cm^2_{Pt}\,cm^{-2}_{MEA}$ (see Fig. 7a) or 50 mA $cm^{-2}_{MEA}$ − 50 mA $cm^{-2}_{Pt}$ for *rf* values <10 $cm^2_{Pt}\,cm^{-2}_{MEA}$ (see Fig. 7b) was used to extrapolate the current density to 0.9 V. Hereby, the lower current density limit was chosen to ensure a ten-fold higher ORR than the $H_2$-crossover current, while the upper limit was chosen to ensure an accurate representation of the first Tafel slope. The obtained current densities normalized to the Pt mass then yield the ORR mass activities ($i^{mass}_{0.9V}$ in $A\,g^{-1}_{Pt}$; normalized to the initial Pt mass in the cathode catalyst layer) or, when normalized to the roughness factor, yield the specific ORR activities ($i^{spec}_{0.9V}$, in mA $cm^{-2}_{Pt}$). Both are summarized in Fig. 8 as a function of *rf*; the gray shaded area indicates *rf* values below 10 $cm^2_{Pt}\,cm^{-2}_{MEA}$, where only semi-quantitative values for *rf* and the ORR activity can be obtained due to large errors in the *ECSA* evaluation (see Fig. 2) and in the extrapolation to 0.9 V. The BoL ORR mass activities of ≈170–200 $A\,g^{-1}_{Pt}$ (left-most points in Fig. 8a) and specific activities of ≈0.24 mA $cm^{-2}_{Pt}$ (left-most points in Fig. 8b) are essentially identical with those reported in a recent voltage cycling study by Padgett et al.[23] for the same catalyst (TEC10V20E from Tanaka), but are ≈30% higher than previously reported by our group (115–135 $A\,g^{-1}_{Pt}$).[10] Over the course of voltage cycling, the mass activity gradually decreased down to ≈27 $A\,g^{-1}_{Pt}$ for the lowest *rf* value of ≈3 $cm^2_{Pt}\,cm^{-2}_{MEA}$. Although a decrease in ORR mass activity with decreasing available Pt surface area is expected,[64] it clearly is not directly proportional to *rf*. After the first 100 aging cycles, an $i^{mass}_{0.9V}$ loss of ≈10% compared to BoL is observed (see second points from the left in Fig. 8a), although the *ECSA* losses and thus the *rf* losses range between ≈15%–25% (see Table II). This is related to an increase in Pt particle size upon voltage cycling, whereby the higher specific activity of larger Pt particles partially compensates for the lower *rf*.[63,64,77] After these first 100 cycles, the mass activity observed in this study agrees reasonably well with the activity observed by Harzer et al. after the same *rf* loss (140–160 $A\,g^{-1}_{Pt}$), indicating that their BoL values were the result of an incomplete activation, as they observed a gain in $i^{mass}_{0.9V}$ in the first 100 cycles.

Over the course of the cycling ASTs, all mass activity curves follow the same trend and show a ≈10-fold reduced mass activity at the lowest measured *rf* values. Again, Padgett et al.[23] reported similar results for $i^{mass}_{0.9V}$ after voltage cycling between 0.6 and 0.95 V using trapezoidal voltage profiles (hold time of 2.5 s and ramp time of 0.5 s), with a remaining mass activity of ≈70 $A\,g^{-1}_{Pt}$ at 24 ± 2% *ECSA* retention (EoL) compared to ≈85 $A\,g^{-1}_{Pt}$ at 20 $cm^2_{Pt}\,cm^{-2}_{MEA}$ (≈25% *ECSA* retention) obtained in this study. This comparability of different aging procedures (trapezoidal vs square wave profiles, and variations in hold time and UPL) used by different groups with

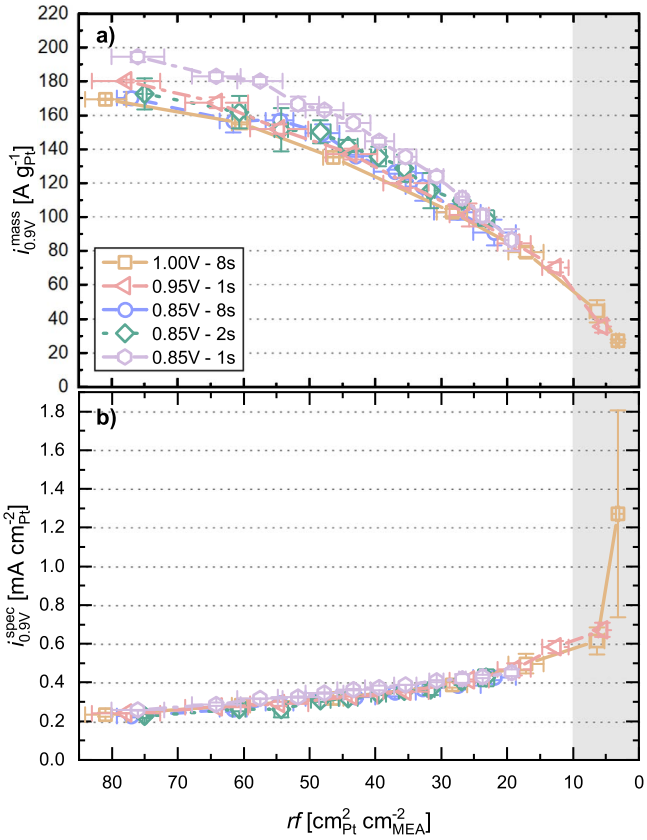


**Figure 8.** Variation of the ORR activity of the cathode catalyst determined at 80 °C, 0.9 V, and 125 kPa $O_2$ partial pressure over the course of voltage cycling ASTs as a function of rf (the left-most values represent BoL): (a) ORR mass activity ($i_{0.9V}^{mass}$) and (b) ORR specific activity ($i_{0.9V}^{spec}$). The ORR activity data were extracted from HFR- and $R_{H^+,\,cath}$-corrected Tafel plots by linear extrapolation to 0.9 V of the data between 50–500 mA $cm_{MEA}^{-2}$ (for rf >10 $cm_{Pt}^{2}$ $cm_{MEA}^{-2}$) or between 50 mA $cm_{MEA}^{-2}$ −50 mA $cm_{Pt}^{-2}$ (for rf <10 $cm_{Pt}^{2}$ $cm_{MEA}^{-2}$ The gray shaded area marks the data for which the rf value and the ORR activity at 0.9 V could only be determined semi-quantitatively. Error bars represent the mean absolute deviation between two independent measurements.

different setups, yielding similar mass activity values at the same *rf* and *ECSA* loss for the same catalyst and catalyst loading, reveals that voltage cycling ASTs under the specified conditions (e.g., UPL ⩽ 1.0 V, no *RH* cycling) result in a similar aging mechanism. The degradation rate can be enhanced with increasing UPL and hold times, but it will reveal similar catalyst characteristics, i.e., essentially identical ORR mass activities at same cathode *rf*, as shown in Fig. 8a.

This conclusion is reinforced by comparing the specific ORR activities for the employed ASTs as a function of cathode *rf* (Fig. 8b). Overall, $i_{0.9V}^{spec}$ increases with decreasing *rf*, which is again consistent with the increase in Pt particle size, as the initially smaller nanoparticles have a large amount of less active edge and corner sites compared to larger particles and thus exhibit lower specific ORR activity.[63,64,77] Again, the values obtained in this study correlate well with other studies, where for a *rf* of ≈20 $cm_{Pt}^{2}$ $cm_{MEA}^{-2}$ the here determined specific activity of ≈0.45 mA $cm_{Pt}^{-2}$ (see Fig. 8b) compares well with those by Padgett et al.[23] (≈0.37 mA $cm_{Pt}^{-2}$) and by Harzer et al.[10] (≈0.43 mA $cm_{Pt}^{-2}$); the BoL values here and in these other two studies are all at ≈0.2 mA $cm_{Pt}^{-2}$.

However, it is surprising that all curves lie perfectly on top of each other. While the same specific activity would be expected for Pt particles of the same size, the *rf* loss is the combined result of Pt loss into the membrane/ionomer phase and a Pt particle size increase due to Oswald ripening. The fact that the same specific activity is observed at identical *rf* values for vastly different aging procedures, e.g., at ≈28 $cm_{Pt}^{2}$ $cm_{MEA}^{-2}$ (corresponding to ≈35% normalized *ECSA* in Fig. 3a) after 1,000 cycles for the 1.00 V–8s AST (orange squares in Fig. 8b) and after 100,000 cycles for the 0.85 V–1s AST (violet hexagon symbols), indicates that they result in the same Pt particle size distribution and that therefore the fraction of Pt lost into the membrane/ionomer phase must be essentially the same for the different ASTs here examined (see Figs. 4c and 4d). Importantly, this implies that the here used voltage cycling ASTs with limited UPL (⩽1.0 V) and nearly full humidification (95% *RH*) accelerate the exact same degradation mechanism, as long as other degradation mechanisms like carbon support corrosion (relevant at UPLs above 1.0 V) and/or ionomer/membrane degradation (relevant at low *RH*) do not play a significant role. As the different UPL values and the hold times should cover reasonably well the transient voltage profiles encountered in PEMFC applications (in the absence of start-up/shut-down events), the very same degradation mechanism would be expected for real applications.

Finally, it needs to be emphasized that the strong and sudden increase in $i_{0.9V}^{spec}$ for very low *rf* values in Fig. 8b (see gray shaded area) is, as discussed above, a likely artefact due to the above discussed measurement uncertainties, so that the respective values should be treated with caution.

***Dependence of $O_2$ transport resistances on cathode rf.***—Based on the established method from Baker et al.,[41] the $O_2$ transport resistances were measured by limiting current measurements over the course of the voltage cycling ASTs (see scheme in Fig. 1). Exemplarily, Fig. 9a shows the limiting current densities ($i_{lim}$) that were recorded at 170 $kPa_{abs}$ for the same MEA at BoL (*rf* ≈ 80 $cm_{Pt}^{2}$ $cm_{MEA}^{-2}$, filled squares) as well as after 2,000 cycles (*rf* ≈ 15 $cm_{Pt}^{2}$ $cm_{MEA}^{-2}$, half-filled triangles) and 10,000 cycles (*rf* ≈ 3 $cm_{Pt}^{2}$ $cm_{MEA}^{-2}$, empty triangles) of the 1.00 V–8s AST procedure. As expected, the limiting current density is nearly vertical for the pristine MEA between 0.2 V and 0.1 V for all oxygen concentrations, and up to 0.3 V for the lower $O_2$ concentration of 2, 4, and 7%. At 0.05 V, the limiting current density slightly increases due to additional hydrogen evolution.[48]

With decreasing *rf*, the now lower currents start to deviate from their potential independence at low potentials. To highlight this, a close-up of the limiting current data for the aged cathode with a remaining *rf* of only ≈3 $cm_{Pt}^{2}$ $cm_{MEA}^{-2}$ is shown in Fig. 9b. Here, a "Z-shape" form of current vs potential is clearly observed for all oxygen concentration, with an apparent minimum value of the currents at ≈0.15–0.2 V. This introduces an obvious ambiguity with regard to the determination of the "correct" limiting current density. Greszler et al. observed similar trends for the limiting current data of a low-loaded MEA with a Pt/Vulcan cathode catalyst (0.03 $mg_{Pt}$ $cm_{MEA}^{-2}$), showing a decrease ("turn-back") in limiting current from 0.2 to 0.1 V, before increasing again below 0.1 V. They attributed this to a transition from the typical four-electron oxygen reduction (water formation) to a two-electron process (hydrogen peroxide formation), which reduces the number of electrons per oxygen molecule and therefore the mass transport limited current density.[48] This is consistent with rotating ring disk electrode measurements by other researchers, who showed an increasing formation of hydrogen peroxide at low potentials with a decrease in *ECSA* (i.e., with decreasing *rf*).[78,79] As this "Z-shape" introduces large ambiguity in the determination of the limiting current density, the maximum current density obtained at potentials >0.1 V (to avoid effects from the hydrogen evolution reaction) was taken in this study as the best possible approximation of the limiting current density. Therefore, the thus estimated $i_{lim}$ value is clearly less than the true $i_{lim}$ value, which in turn means that it will lead to an overestimation of the $O_2$ transport resistance (see below).

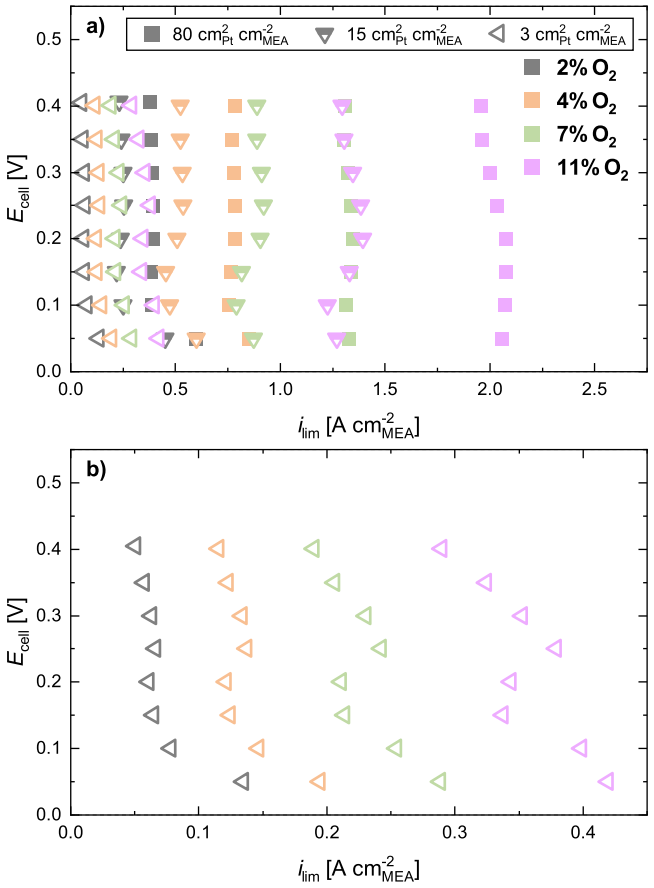


**Figure 9.** (a) Limiting current measurement in the potential range between 0.40 V and 0.05 V using $O_2$ concentrations of 2% (gray), 4% (orange), 7% (green) and 11% (magenta) in $N_2$ (on a dry gas basis) for a representative cathode at BoL (≈80 $cm^2_{Pt}\,cm^{-2}_{MEA}$, filled squares), after 2,000 cycles (≈15 $cm^2_{Pt}\,cm^{-2}_{MEA}$; half-filled triangles), and after 10,000 cycles (≈3 $cm^2_{Pt}\,cm^{-2}_{MEA}$, empty triangles) of the 1.00 V–8s voltage cycling AST. (b) Zoomed-in view at low current densities for the data after 10,000 cycles (≈3 $cm^2_{Pt}\,cm^{-2}_{MEA}$), showing a pronounced "Z-shape." The measurements were performed at 170 $kPa_{abs}$, 80 °C, and 95% RH using 2000 nccm $H_2$ and 5000 nccm ($O_2$ in $N_2$) on anode and cathode, respectively.

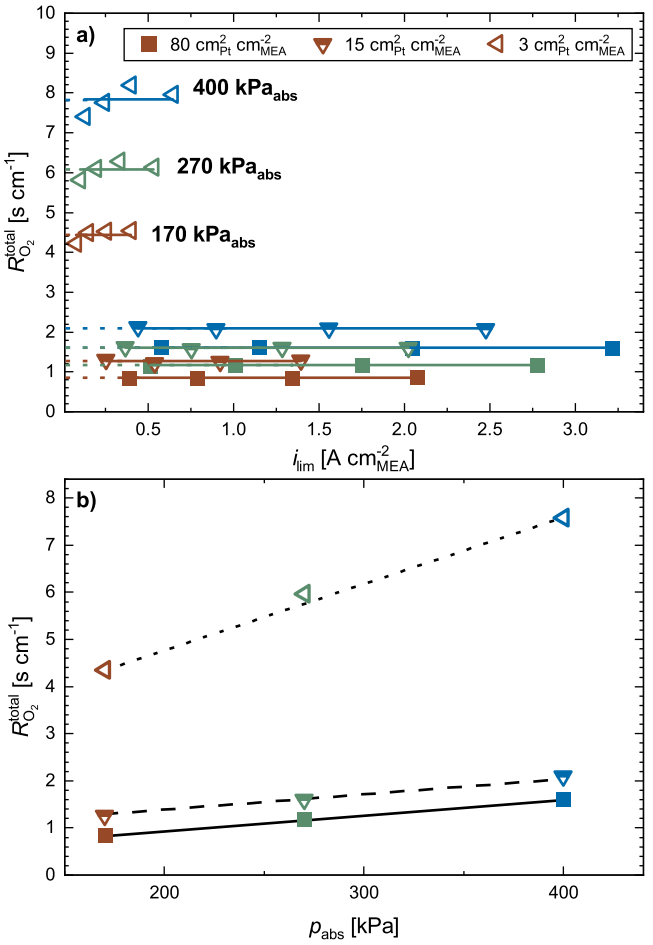


**Figure 10.** (a) Total $O_2$ transport resistance ($R_{O_2}^{total}$) vs limiting current density ($i_{lim}$) for a representative cathode at BoL (≈80 $cm^2_{Pt}\,cm^{-2}_{MEA}$, filled squares), after 2,000 cycles (≈15 $cm^2_{Pt}\,cm^{-2}_{MEA}$; half-filled triangles), and after 10,000 cycles (≈3 $cm^2_{Pt}\,cm^{-2}_{MEA}$, empty triangles) of the 1.00 V–8s voltage cycling procedure (same as in Fig. 9), recorded at pressures of 170, 270, and 400 $kPa_{abs}$ with 2, 4, 7, and 11% $O_2$ in $N_2$ (dry gas basis). The measurements were performed at 80 °C and 95% RH, and the horizontal lines show the averaged values of $R_{O_2}^{total}$ for the various conditions. (b) Plot of $R_{O_2}^{total}$ of the different cathodes as a function of pressure, used for the deconvolution of $R_{O_2}^{total}$ into a pressure-dependent ($R_{O_2}^{PD}$) and a pressure-independent ($R_{O_2}^{PI}$) term according to Baker et al.[41]

At each pressure, the total $O_2$ transport resistance ($R_{O_2}^{total}$) was then calculated from the determined/approximated limiting currents ($i_{lim}$) at each oxygen concentration ($c_{O_2}$) according to Eq. 3, where $F$ is the faradaic constant (96485 C $mol^{-1}$);[41]

$$R_{O_2}^{total} = \frac{4Fc_{O_2}}{i_{lim}} \quad [3]$$

For low oxygen concentrations, the transport mechanism is generally characterized by oxygen transport in the so-called "dry region,"[80] in which $R_{O_2}^{total}$ vs the limiting current density is constant and therefore independent of the oxygen concentration at any given pressure. This independence of $R_{O_2}^{total}$ vs $i_{lim}$ (and vs $c_{O_2}$) can be seen in Fig. 10a for the BoL data with $rf \approx 80$ $cm^2_{Pt}\,cm^{-2}_{MEA}$ (solid squares), marked by the horizontal lines for each pressure (the corresponding $i_{lim}$ data at 170 $kPa_{abs}$ are shown in Fig. 9a). The same is observed for the MEA after 2,000 cycles of the 1.00 V–8s voltage cycling AST ($rf$≈15 $cm^2_{Pt}\,cm^{-2}_{MEA}$; half-filled triangles). However, after 10,000 cycles of the 1.00 V–8s AST ($rf$≈3 $cm^2_{Pt}\,cm^{-2}_{MEA}$, empty triangles), this independence of $R_{O_2}^{total}$ on $i_{lim}$ is not anymore observed, and the $R_{O_2}^{total}$ data show a significant scatter. This must be due to the above described issue that the true value of $i_{lim}$ cannot be reliably determined at low $rf$ values, so that the estimated $R_{O_2}^{total}$ values only represent their uppermost limit.

According to Baker et al., the total $O_2$ transport resistance can be divided in a pressure-independent contribution ($R_{O_2}^{PI}$) and a pressure-dependent contribution ($R_{O_2}^{PD}$) via a linear regression of $R_{O_2}^{total}$ vs the absolute pressure (see Fig. 10b).[41] The pressure-independent $O_2$ transport resistance consists of various contributions, namely Knudsen diffusion in the small pores of the catalyst layer and the microporous layer (MPL) as well as the so-called local $O_2$ resistance ($R_{O_2}^{local}$), which is a function of $rf$ and that is often associated to diffusion in the ionomer and liquid water phase.[48,69,73,81] On the other hand, the pressure-dependent transport resistance is mostly associated with the molecular diffusion of $O_2$ in the GDL and, in part, in the MPL and in the catalyst layer. $R_{O_2}^{PD}$ is therefore expected to remain constant as long as the pore structure of GDL, MPL, and catalyst layer are not affected, i.e., in the absence of conditions that lead to a corrosion of the catalyst carbon support (or the MPL/GDL). Since $R_{O_2}^{PD}$ is characterized by the slope of $R_{O_2}^{total}$ as a function of pressure, the slope is expected to remain constant throughout the

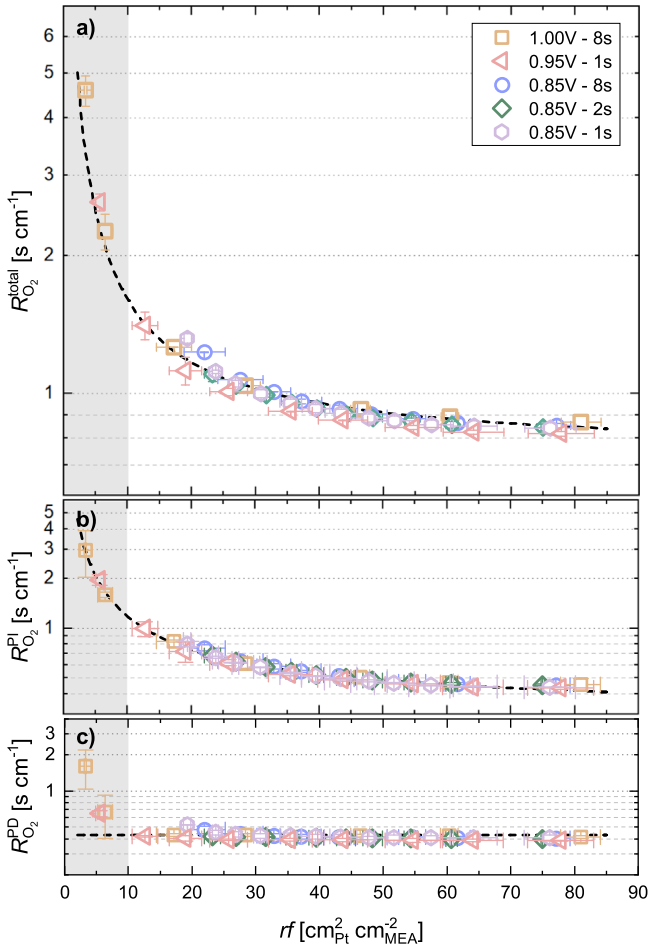


**Figure 11.** Variation of the $O_2$ mass transport resistance at 170 $kPa_{abs}$ with the cathode rf value over the course of the different voltage cycling ASTs: (a) total $O_2$ transport resistance ($R_{O_2}^{total}$), (b) pressure-independent $O_2$ transport resistance ($R_{O_2}^{PI}$), and (c) pressure-dependent $O_2$ transport resistance ($R_{O_2}^{PD}$). The dashed black line in panel c corresponds to the averaged $R_{O_2}^{PD}$ value of 0.42 ± 0.02 s cm$^{-1}$ (excluding the data in the gray shaded area). The dashed black line in panel b represents the fit of the $R_{O_2}^{PI}$ data to Eq. 4 (excluding data in the gray shaded area), yielding $R_{O_2}^{PI}|_{rf\to\infty} = 0.32 \pm 0.01$ s cm$^{-1}$ and $R_{O_2}^{local} = 8.6 \pm 0.2$ s cm$^{-1}$. The dashed black line in panel a is based on Eq. 5, using the above determined values of $R_{O_2}^{PD}$, $R_{O_2}^{PI}|_{rf\to\infty}$, and $R_{O_2}^{local}$ to calculate $R_{O_2}^{total}$ vs cathode *rf*. The gray shaded area marks the *rf* region for which the calculated $O_2$ transport resistances are considered inaccurate due to the undefined limiting current values (see Fig. 9b) and the higher errors in the determination of the cathode rf values (see Fig. 2).

aging, which is observed as long as $R_{O_2}^{total}$ could be determined reliably, i.e., for *rf* > 10 $cm^2_{Pt}$ $cm^{-2}_{MEA}$ (see half-filled triangles and solid squares in Fig. 10b). However, data for the MEAs with a lower *rf* did not fit the linear model quite as good, and the slope is much higher (empty triangles in Fig. 10b).

The obtained values for $R_{O_2}^{total}$, $R_{O_2}^{PI}$, and $R_{O_2}^{PD}$ at 170 $kPa_{abs}$ vs cathode *rf* over the course of the different voltage cycling ASTs are summarized in Fig. 11. Quite strikingly, the values for the oxygen transport related resistances do not depend on the aging procedure but exclusively depend on the cathode *rf*, thereby again suggesting that the different here examined voltage cycling ASTs apparently induce the same degradation mechanism. Over the course of aging, i.e., with decreasing cathode *rf*, the total oxygen transport resistance increases (Fig. 11a), similar to the increase of $R_{O_2}^{total}$ with decreasing cathode catalyst loading (i.e., with decreasing cathode *rf*) that was observed by Greszler et al.[48] On the other hand, $R_{O_2}^{PD}$ remains essentially constant for all *rf* values of >10 $cm^2_{Pt}$ $cm^{-2}_{MEA}$ (Fig. 11c), as would be expected under conditions where the corrosion of the cathode catalyst carbon support is negligible (i.e., for UPL ⩽1.0 V); the apparent increase of $R_{O_2}^{PD}$ at lower *rf* values (data points in the gray shaded area in Fig. 11c) is, we believe, caused be the large errors in the quantification of $i_{lim}$ (see Fig. 9b) and *rf* (see Fig. 2) at very low *rf* values (further substantiated below). An analogous increase of $R_{O_2}^{PD}$ with decreasing cathode *rf* was also observed in other voltage cycling AST studies[10] as well as for pristine MEAs that were prepared with different catalysts and/or different catalyst loadings[18] (i.e., with different BoL cathode *rf*).

Therefore, Fig. 11 shows that the increase in $R_{O_2}^{total}$ with decreasing cathode *rf* is mainly the result of an increasing $R_{O_2}^{PI}$ (see Fig. 11b), which in turn results from the *rf*-dependent contribution of the so-called local $O_2$ resistance ($R_{O_2}^{local}$).[10,17,48] As mentioned earlier, the contribution of $R_{O_2}^{local}$ has been reported to be inversely proportional to *rf*.[48] It is therefore possible to disentangle the *rf*-independent fraction of $R_{O_2}^{PI}$, namely the Knudsen diffusion in catalyst layer and MPL that would still be expected for a hypothetical infinite cathode *rf* ($R_{O_2}^{PI}|_{rf\to\infty}$), and $R_{O_2}^{local}$ by fitting $R_{O_2}^{PI}$ to Eq. 4:

$$R_{O_2}^{PI} = R_{O_2}^{PI}|_{rf\to\infty} + \frac{R_{O_2}^{local}}{rf} \quad [4]$$

A least-squares fit of all the measured $R_{O_2}^{PI}$ data for a cathode *rf* of >10 $cm^2_{Pt}$ $cm^{-2}_{MEA}$ (i.e., excluding the data in the gray shaded area in Fig. 11) is given by the black dashed line in Fig. 11b, whereby a *rf*-independent fraction of $R_{O_2}^{PI}|_{rf\to\infty} = 0.32 \pm 0.01$ s cm$^{-1}$ and a local oxygen transport resistance of $R_{O_2}^{local} = 8.6 \pm 0.2$ s cm$^{-1}$ were obtained. This $R_{O_2}^{local}$ value at 80 °C and 95% *RH* agrees reasonably well with the local oxygen transport resistance of ≈12 s cm$^{-1}$ that was obtained at 80 °C and 62% *RH* by Greszler et al.,[48] perhaps suggesting a slight decrease of $R_{O_2}^{local}$ with *RH*. According to the above discussion, an average $R_{O_2}^{PD}$ of 0.42 ± 0.02 s cm$^{-1}$ (indicated by the dashed black line in Fig. 11c) was obtained at 170 $kPa_{abs}$ for all data points (excluding those in the gray shaded area). Taking all of these observations into account, the pressure- and *rf*-dependence of the total $O_2$ transport resistance can be summarized by Eq. 5 (dashed line in Fig. 11a):

$$R_{O_2}^{total} = R_{O_2}^{PD} + R_{O_2}^{PI} = R_{O_2}^{PD} + R_{O_2}^{PI}|_{rf\to\infty} + \frac{R_{O_2}^{local}}{rf} \quad [5]$$

Using the above determined values of $R_{O_2}^{PD}$, $R_{O_2}^{PI}|_{rf\to\infty}$, and $R_{O_2}^{local}$, the values of $R_{O_2}^{total}$ vs *rf* calculated by Eq. 5 are shown by the black dashed line in Fig. 11a. Even at values that were excluded from the fits because the determination of $i_{lim}$ was deemed unreliable at *rf* <10 $cm^2_{Pt}$ $cm^{-2}_{MEA}$ (gray shaded area in Fig. 11), the $R_{O_2}^{total}$ values predicted by Eq. 5 represent the measured $R_{O_2}^{total}$ values surprisingly well. It can therefore be concluded that although the limiting current measurements for severely degraded cathodes (i.e., cathodes with *rf* <10 $cm^2_{Pt}$ $cm^{-2}_{MEA}$) are prone to errors due to the increasing impact of HER currents and a possible $H_2O_2$ reaction pathway, a reasonably accurate experimental quantification of $R_{O_2}^{total}$ seems to be still possible but that a distinction between $R_{O_2}^{PI}$ and $R_{O_2}^{PD}$ is not.

***Dependence of the H₂/air performance on cathode.***—As discussed above, the $H_2$/air performance deteriorates over the course of a voltage cycling AST (see Fig. 5), owing to a combination of decreasing Pt *ECSA* (see Fig. 3), decreasing ORR mass activity (see Fig. 8a), and increasing oxygen transport resistance (see Fig. 11).

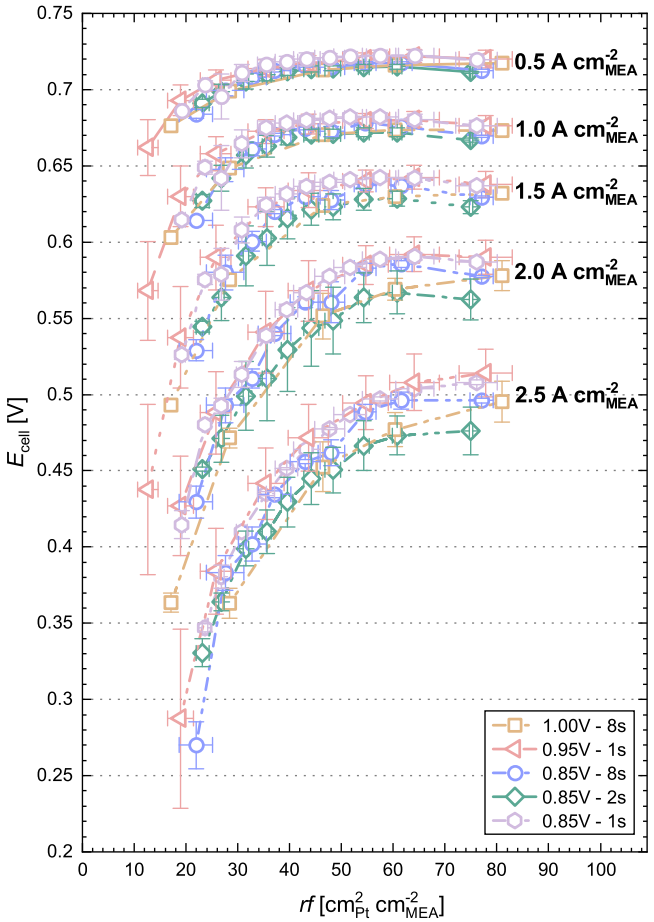


**Figure 12.** Measured cell voltages in differential flow $H_2$/air polarization curves for various geometric current densities (0.5, 1.0, 1.5, 2.0, and 2.5 A $cm^{-2}_{MEA}$) as a function of cathode rf over the course of the different voltage cycling ASTs (see legend in the figure). The measurements were performed in $H_2$/air (2000/5000 nccm) at 170 $kPa_{abs}$, 80 °C, and 95% RH (cell voltages for $rf < 10$ $cm^2_{Pt}$ $cm^{-2}_{MEA}$ are not shown). The BoL performance corresponds to the right-most data point for each AST procedure, and error bars represent the mean absolute deviation between two independent measurements.

Based on the pronounced correlation of all the investigated voltage loss contributions with cathode *rf* (except for the *HFR* and the cathode proton conduction resistance, which are unaffected by voltage cycling), this section now aims to correlate the PEMFC performance in $H_2$/air with the cathode *rf*.

Figure 12 shows the measured $H_2$/air cell voltages at different geometric current densities as a function of *rf*, plotting the data obtained over the course of all of the five examined voltage cycling ASTs (see Table I). Overall, it can be seen for each current density that the measured cell voltages match surprisingly well between the different AST protocols (see Table IV), whereby the scatter between the measurements is mostly the result of variations in the BoL performance (see right-most data points in Fig. 12, with the largest BoL performance deviation observed for the MEAs used for the 0.85 V–2s AST (green diamonds)). As discussed in the preceding sections, ORR mass activities and oxygen mass transport resistances solely depend on the cathode *rf*, so that also the kinetic and transport induced overpotentials must be exclusive functions of the cathode *rf*. Especially in the high current density region, the $H_2$/air cell voltage is most strongly affected by the oxygen mass transport resistance that increases with decreasing cathode *rf*, as seen for the highest current density (i.e., at 2.5 *A* $cm^{-2}_{MEA}$; lowermost curve in Fig. 12), where the $H_2$/air cell voltage curve already starts to bend downwards once the roughness factor has decreased to ≈55 $cm^2_{Pt}$ $cm^{-2}_{MEA}$ (corresponding to an *ECSA*/*rf* loss of ≈30%). At a cathode *rf* of ≈30 $cm^2_{Pt}$ $cm^{-2}_{MEA}$, the average cell voltage loss at 2.5 A $cm^{-2}_{MEA}$ compared to BoL already amounts to ≈100 mV (see last row in Table IV). In contrast, at low current densities (e.g., 0.5 A $cm^{-2}_{MEA}$; uppermost curves in Fig. 12), the performance losses are mostly governed by ORR mass activity losses and the $H_2$/air cell voltage remains therefore rather constant up to low *rf* values, amounting to only ≈10 mV at ≈30 $cm^2_{Pt}$ $cm^{-2}_{MEA}$ (see second row in Table IV). However, even at 0.5 *A* $cm^{-2}_{MEA}$, substantial mass transport losses become apparent below *rf* ≈ 30 $cm^2_{Pt}$ $cm^{-2}_{MEA}$, as indicated by the sharp downturn of the cell voltage curve.

All in all, a surprisingly universal correlation between $H_2$/air performance and cathode *rf* was found for the five different voltage cycling ASTs with upper potentials between 0.85 and 1.0 V and with hold times of 1 to 8 s. This strongly suggests that the governing aging mechanisms are the same under the here chosen conditions (viz., Pt dissolution/redeposition), which however should represent those in actual PEMFC systems in the absence of start-up/shut-down events and ionomer degradation. Under these constraints (no start-up/shut-down events and high *RH* to avoid chemical degradation of the ionomer), this correlation should allow for the prediction of voltage losses arising from load cycling.

***Voltage cycling induced $H_2$/air performance loss prediction over large cycle numbers.***—For the examined upper potential limits (0.85–1.0 V) and hold times (1–8 s), the above analysis shows that the cathode *rf* loss uniquely governs the loss in $H_2$/air performance (see Fig. 12). This can be used to project the voltage cycling induced $H_2$/air performance losses up to very large cycle numbers under application-relevant conditions where the degradation is slow (e.g., low UPL values), considering the following two observations: (i) The empirical correlation that the cathode *rf* (or *ECSA*) after the first 100 cycles decreases linearly with the logarithm of the cycle number (until *rf* ≈ 10 $cm^2_{Pt}$ $cm^{-2}_{MEA}$; see Fig. 3a), so that the change of *ECSA*/*rf* can be extrapolated over quite a large cycle number range; (ii) The finding that the cathode *rf* loss can be accelerated by high UPL values (but restricted to ⩽1.0 V in order to avoid carbon corrosion) and by shorter hold times (down to 1 s) without affecting the $H_2$/air performance vs cathode *rf* correlation (see Fig. 12).

Based on these observations, we propose a novel approach to predict the load cycling limited lifetime of MEAs based on two sets of measurements, which is schematically depicted in Fig. 13. In order to reduce the measurement time that would be required to determine the voltage cycling induced degradation under application-relevant operating conditions (i.e., UPL < 0.9 V), a voltage cycling AST is first conducted under harsh cycling conditions (i.e., 0.95–1.0 V UPL and 1 s hold time), thereby enabling a characterization of the full *rf* range down to low *rf* values within a low number of cycles that require relatively little measurement time (see step 1 in Fig. 13a). In a second set of measurements, an application-relevant voltage cycling protocol (i.e., with a UPL of 0.85 V or below) is employed to determine the characteristic cathode *rf* degradation rate under application-relevant conditions (step 2 in Fig. 13a). This procedure is performed within a limited experimental time frame, whereby it is essential that the cathode *rf* degradation rate after the initial procedure-independent settle-in phase (i.e., an *ECSA* loss of ≈15%–20%, which with the here used Pt/Vulcan catalyst occurs after the first 100 cycles) is determined with great accuracy; subsequently, the voltage cycling procedure is continued until a cathode *rf* loss of ≈40%–50% is obtained. In this case, the cathode *rf* loss for a larger number of cycles can then be predicted by linear extrapolation of cathode *rf* vs the logarithm of the cycle number (step 3 in Fig. 13a), which has been observed to hold until ≈10%–15% of the initial cathode *ECSA* value (see Fig. 3). It should be noted that the settle-in phase is greatly important for this analysis: e.g., one could think of two (hypothetical) electrodes that have the same characteristic slope and *rf* value after the initial settle-in phase,

**Table IV. Cell voltages obtained from $H_2$/air performance measurements at geometric current densities of 0.5, 1.5, and 2.5 A $cm^{-2}_{MEA}$ for high, medium, and low cathode rf values, averaged over all measurements, i.e., over 5 different ASTs (see Table I) and two independent measurements per AST protocol. The given variation represents the standard deviation of the in total 10 independent measurements.**

| rf [$cm^2_{Pt}$ $cm^{-2}_{MEA}$] | $E_{cell}$ at 0.5 A $cm^{-2}_{MEA}$ | $E_{cell}$ at 1.5 A $cm^{-2}_{MEA}$ | $E_{cell}$ at 2.5 A $cm^{-2}_{MEA}$ |
|---|---|---|---|
| 77.4 ± 3.3 (BoL) | 716 ± 5 mV | 632 ± 7 mV | 498 ± 16 mV |
| 49.2 ± 3.6 | 717 ± 4 mV | 633 ± 8 mV | 470 ± 17 mV |
| 30.2 ± 3.2 | 705 ± 8 mV | 592 ± 20 mV | 395 ± 24 mV |

but in one case, this initial phase might require 10 times more cycles, resulting in a right-shift of the blue curve in Fig. 13a by one order of magnitude, and therefore in a 10-fold higher cycle number to reach a cathode *rf* loss of ≈40%-50% (this will be shown in a future publication).

The harsh AST experiment (purple symbols in Fig. 13a) should provide a good estimate of the $H_2$/air performance vs cathode *rf* throughout the whole *rf* range (exemplarily shown in Fig. 13b for 1.0 and 2.0 A $cm^{-2}_{MEA}$). This means that the expected *rf* for a defined EoL performance, e.g., 0.5 V at 2.0 A $cm^{-2}_{MEA}$ (pink shaded area in Fig. 13b, step 4), can be extracted from the $H_2$/air cell voltage (at defined current densities) vs *rf* curve obtained for the harsh AST. In the example given in Fig. 13, this target of 0.5 V at 2.0 A $cm^{-2}_{MEA}$ would correspond to a final cathode *rf* of ≈27 $cm^2_{Pt}$ $cm^{-2}_{MEA}$ (pink area, step 5 in Fig. 13b). Finally, the projected number of cycles after which the EoL criteria of 0.5 V at 2.0 A $cm^{-2}_{MEA}$ would be expected to be reached for the application-relevant (i.e., less harsh) voltage cycling protocol is obtained by extrapolating the cathode *rf* vs logarithm of the cycle number line to the same *rf* of ≈27 $cm^2_{Pt}$ $cm^{-2}_{MEA}$ (crossing of the blue dashed line and the pink area in Fig. 13a; step 6), which in this example would be ≈300,000 cycles. As mentioned above, this is only valid if all other degradation mechanisms can be considered negligible.

***Expected behavior for different MEA types and different AST conditions.***—While this study did not investigate the dependence of the performance degradation over the course of voltage cycling ASTs conducted at different temperature, *RH*, lower potential limit, cathode gas composition ($N_2$ or air), or voltage cycle profiles, the impact of these factors is generally well understood.[8–10,65,82,83] Thus, it seems reasonable to assume that a linear behavior of the cathode *rf* vs the logarithm of the cycle number and the observed unique $H_2$/air performance vs *rf* profile will be observed for other voltage cycling AST protocols with the same cathode electrode *as long as* the degradation is dominated by the platinum dissolution/redeposition mechanism. This should be the case within the following boundary conditions: (i) the UPL is low enough that the carbon corrosion rate at the respective temperature is negligible over the experiment duration;[84,85] (ii) chemical degradation of the ionomer/membrane that occurs during $H_2$/air operation at low *RH* is avoided; (iii) mechanical and thermal degradation of the ionomer/membrane is prevented (limited number of *RH* cycles and operating temperatures <150 °C);[86] and (iv) absence of carbon support corrosion due to start-up/shut-down or (local) $H_2$ starvation events.[3,5,84–86] Within these restrictions, it should be possible to determine accelerating factors for a wide range of voltage/load cycling conditions by comparing the characteristic slopes for the same BoL configuration, i.e., the same MEA composition (particularly with respect to the cathode catalyst and the ionomer type/content in the cathode electrode) and the same cell hardware.

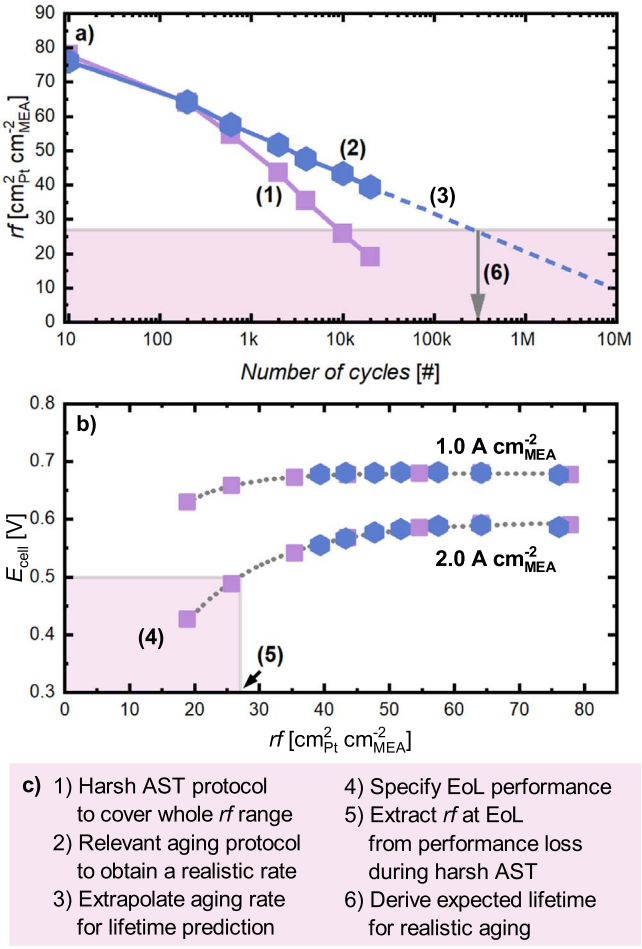


**Figure 13.** Scheme of the proposed approach to predict the voltage cycling losses of the $H_2$/air performance over a large number of voltage cycles under application-relevant conditions (i.e., UPLs of <0.9 V) based on the data acquired for a harsh cycling protocol (i.e., conducted with an UPL of 0.95–1.0 V). (a) Cathode *rf* degradation for a harsh voltage cycling AST (purple squares) and for an application-relevant "mild" voltage cycling AST (blue hexagons). (b) $H_2$/air performance as a function of cathode *rf* for two current densities. (c) Outline of the step-wise procedure to estimate the number of cycles after which the EoL criteria (here assumed to be 0.5 V at 2 A $cm^{-2}_{MEA}$) are reached for the mild voltage cycling AST on the basis of the harsh voltage cycling AST data. The actual data points are taken from the 0.95 V–1s AST (purple squares) and from the 0.85 V–1s AST (blue hexagons).

Similarly, it should be possible to compare the degradation for different cathode electrodes, (i.e., with regard to the carbon support morphology of the catalyst, the Pt content and the Pt particle size distribution of the catalyst, the ionomer type/content, the electrode thickness, or the Pt loading) by employing the same set of voltage cycling AST protocols. However, it should be noted that the individual voltage loss contributions and therefore the $H_2$/air performance of an MEA depend strongly on the above listed cathode electrode properties (as well as the membrane type/thickness), so that one would expect to obtain different absolute values when plotting the $H_2$/air cell voltages at different geometric current densities as a function of *rf* for different MEA types (e.g., a Ketjenblack supported catalyst will have a higher ORR activity but worse $O_2$-transport properties compared to a Vulcan supported catalyst with the same *ECSA*[17]). Still, the trend of a quickly decaying cell voltage at high current densities compared to a mostly maintained low current density performance with decreasing cathode *rf* (confer Fig. 12) would be expected to be the same for different MEA types. Due to the anisotropic nature of the Pt dissolution/

redeposition mechanism in the through-plane direction of the electrode (see Fig. 4), differences in the $H_2$/air performance vs *rf* correlation would also be expected when two different cathode loadings of the same catalyst are compared (corresponding to different electrode thicknesses), although the differences would most likely be less pronounced than for MEAs with different cathode catalysts. Therefore, the here observed characteristic correlation between the $H_2$/air performance and the cathode *rf* over the course of voltage cycling ASTs needs to be established for each MEA type, whereby the $H_2$/air cell voltage is furthermore affected by the other cell components (e.g., GDL type and compression, and flow field design) and by the operating conditions during the $H_2$/air performance measurements (temperature, pressure, *RH*, reactant stoichiometry, etc.).

## Conclusions

In this study, the degradation of PEMFC cathodes with a loading of 0.1 $mg_{Pt}\ cm^{-2}_{MEA}$ was investigated by square wave voltage cycling profiles between 0.6 V and different upper potential limits (UPLs of 0.85, 0.95, and 1.0 V) under $H_2/N_2$ (anode/cathode) with hold times at the vertex potentials of 1, 2, or 8 s. Similar to other studies, it was found that aging protocols with higher UPL and longer hold times induce higher cathode roughness factor (*rf*) or electrochemically active surface area (*ECSA*) losses per cycle, resulting in faster $H_2$/air performance degradation. After a mostly AST-independent *ECSA* (or cathode *rf*) loss in the first 100 cycles, a linear trend of the *ECSA* (or cathode *rf*) loss was observed in plots of the *ECSA* vs the logarithm of either the number of cycles or the time at UPL. This linearity can be used to predict the *ECSA* (or cathode *rf*) loss after extended cycling by an extrapolation of the trend line.

When investigating the individual voltage loss contributions that govern the $H_2$/air performance over the course of the various voltage cycling ASTs, it was found that the $H_2$-crossover, the *HFR*, and the proton conduction resistance remain unchanged, while the ORR mass and specific activity as well as the oxygen transport resistances correlate exclusively with the cathode *rf*, independent of the voltage cycling procedure (i.e., independent of the investigated UPLs and the hold times). This shows that the degradation mechanism is identical for the different AST conditions used in this study, and is restricted to Pt dissolution/redeposition, as cathode catalyst carbon support at UPLs $\leqslant$1.0 V and chemical ionomer degradation under nearly fully humidified conditions (95% *RH*) are negligible. As expected, the ORR mass activity decreased with decreasing cathode *rf*, while the specific activity increased due to the particle size effect. The pressure-independent part of the $O_2$ transport resistance was shown to be strongly affected by the local $O_2$ transport resistance that scales with $rf^{-1}$, whereas the pressure-dependent $O_2$ transport resistance remained unchanged over the course of the ASTs. For all measurements, a *rf* of $\approx$10 $cm^2_{Pt}\ cm^{-2}_{MEA}$ proved to be a critical value, below which a reliable determination of the ORR mass activity and the oxygen mass transport resistances was no longer possible.

The fact that the decrease of the ORR mass activity and the increase of the $O_2$ transport resistances with decreasing cathode *rf* is identical for the here examined five different voltage cycling ASTs, explains the at first sight surprising observation that the $H_2$/air performance decreases with decreasing cathode *rf* is also identical for all five voltage cycling ASTs. In combination with the linear behavior of the cathode *rf* losses vs the logarithm of the cycle number, these findings can be used to predict the voltage cycling losses of the $H_2$/air performance over a large number of voltage cycles under application-relevant conditions (i.e., UPLs of $<$0.9 V) based on the data acquired for a harsh cycling protocol (i.e., conducted with an UPL of 0.95–1.0 V).

## Acknowledgments

We would like to express our gratitude to Katia Rodewald for measuring the SEM micrographs of MEA cross-sections. Financial support in the frame of the POREForm project funded by the German Federal Ministry for Economic Affairs and Energy (BMWi; funding number 03ET B027C) is gratefully acknowledged.

## Appendix

In order to determine whether there is any cathode thinning due to carbon support corrosion after 500,000 voltage cycles using the 0.85 V–1s AST protocol, the cathode electrode thickness was evaluated from ion-milled cross-sections of MEAs at BoL and after 500,000 cycles of the 0.85 V–1s AST. Representative cross-sections are shown in Fig. A·1.

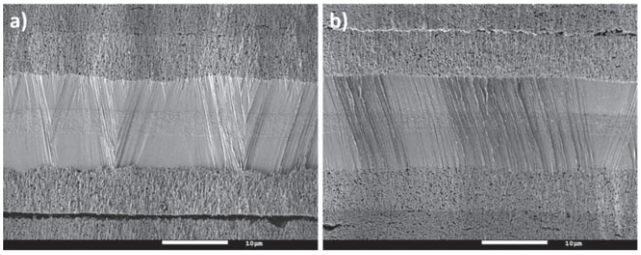


**Figure A·1.** Representative SEM micrograph of ion-milled MEA cross-sections (a) after BoL characterization and (b) after 500,000 voltage cycles using the 0.85 V–1s AST protocol. While the GDL was peeled off before the polishing step, some MPL residuals are still observed in the SEM images, directly above or below the cathode/anode (top/bottom) electrode for both MEAs. The white scale bar at the bottom of each image represents 10 $\mu$m.

## ORCID

Roberta K. F. Della Bella https://orcid.org/0000-0002-3085-3536
Björn M. Stühmeier https://orcid.org/0000-0001-7713-2261
Hubert A. Gasteiger https://orcid.org/0000-0001-8199-8703

## References

1. *Fuel Cell Technologies Program Multi-Year Research, Development, and Demonstration Plan - 3.4 Fuel Cells*, U.S. Department of Energy (2017), accessed: 11/12/2021, https://www.energy.gov/eere/fuelcells/downloads/hydrogen-and-fuel-cell-technologies-office-multi-year-research-development.
2. R. L. Borup, A. Kusoglu, K. C. Neyerlin, R. Mukundan, R. K. Ahluwalia, D. A. Cullen, K. L. More, A. Z. Weber, and D. J. Myers, *Curr. Opin. Electrochem.*, **21**, 192 (2020).
3. T. Patterson and R. Darling, *Electrochem. Solid-State Lett.*, **9**, A183 (2006).
4. P. J. Ferreira, G. J. la O', D. Shao-Horn, R. Morgan, S. K Makharia, and H. A. Gasteiger, *J. Electrochem. Soc.*, **152**, A2256 (2005).
5. C. A. Reiser, L. Bregoli, T. W. Patterson, J. S. Yi, J. D. Yang, M. L. Perry, and T. D. Jarvi, *Electrochem. Solid-State Lett.*, **8**, A273 (2005).
6. L. Dubau, L. Castanheira, and F. Maillard et al., "A review of PEM fuel cell durability: materials degradation, local heterogeneities of aging and possible mitigation strategies." *WIREs Energy Environ.*, **3**, 540 (2014).
7. J. Wu, X. Z. Yuan, J. J. Martin, H. Wang, J. Zhang, J. Shen, S. Wu, and W. Merida, *J. Power Sources*, **184**, 104 (2008).
8. P. Zihrul, I. Hartung, S. Kirsch, G. Huebner, F. Hasché, and H. A. Gasteiger, *J. Electrochem. Soc.,*, **163**, F492 (2016).
9. A. Kneer and N. Wagner, *J. Electrochem. Soc.,*, **166**, F120 (2019).
10. G. S. Harzer, J. N. Schwämmlein, A. M. Damjanović, S. Ghosh, and H. A. Gasteiger, *J. Electrochem. Soc.,*, **165**, F3118 (2018).
11. D. J. S. Sandbeck, N. M. Secher, F. D. Speck, J. E. Sørensen, J. Kibsgaard, I. Chorkendorff, and S. Cherevko, *ACS Catal.*, **10**, 6281 (2020).
12. K. Yu, D. J. Groom, X. Wang, Z. Yang, M. Gummalla, S. C. Ball, D. J. Myers, and P. J. Ferreira, *Chem. Mater.*, **26**, 5540 (2014).
13. R. Makharia, S. Kocha, P. Yu, M. Sweikart, W. Gu, F. Wagner, and H. A. Gasteiger, *ECS Transaction*, **1**, 3 (2006).
14. E. Antolini, *Appl. Catal., B*, **181**, 298 (2016).
15. D. J. S. Sandbeck et al., *J. Electrochem. Soc.*, **167**, 164501 (2020).
16. A. Kneer, J. Jankovic, D. Susac, A. Putz, N. Wagner, M. Sabharwal, and M. Secanell, *J. Electrochem. Soc.*, **165**, F3241 (2018).
17. V. Yarlagadda, M. K. Carpenter, T. E. Moylan, R. S. Kukreja, R. Koestner, W. Gu, L. Thompson, and A. Kongkanand, *ACS Energy Lett.*, **3**, 618 (2018).
18. A. Kongkanand and M. F. Mathias, *J. Phys. Chem. Lett.*, **7**, 1127 (2016).
19. J. P. Owejan, J. E. Owejan, and W. Gu, *J. Electrochem. Soc.*, **160**, F824 (2013).
20. P. Urchaga, T. Kadyk, S. G. Rinaldo, A. O. Pistono, J. Hu, W. Lee, C. Richards, M. H. Eikerling, and C. A. Rice, *Electrochim. Acta*, **176**, 1500 (2015).
21. D. J. Myers, X. Wang, M. C. Smith, and K. L. More, *J. Electrochem. Soc.*, **165**, F3178 (2018).

22. Y. Hu, J. O. Jensen, P. Bretzler, L. N. Cleemann, J. Yu, and Q. Li, *Electrochim. Acta*, **391**, 138963 (2021).
23. E. Padgett et al., *J. Electrochem. Soc.,*, **166**, F198 (2019).
24. A. Kneer, N. Wagner, C. Sadeler, A.-C. Scherzer, and D. Gerteisen, *J. Electrochem. Soc.,*, **165**, F805 (2018).
25. S. Stariha, N. Macauley, B. T. Sneed, D. Langlois, K. L. More, R. Mukundan, and R. L. Borup, *J. Electrochem. Soc.*, **165**, F492 (2018).
26. D. A. Langlois, A. S. Lee, N. Macauley, S. Maurya, M. E. Hawley, S. D. Yim, and Y. S. Kim, *J. Power Sources*, **396**, 345 (2018).
27. N. Ramaswamy, S. Kumaraguru, W. Gu, R. S. Kukreja, K. Yu, D. Groom, and P. Ferreira, *J. Electrochem. Soc.*, **168**, 024519 (2021).
28. D. D. Papadias, R. K. Ahluwalia, N. Kariuki, D. Myers, K. L. More, D. A. Cullen, B. T. Sneed, K. C. Neyerlin, R. Mukundan, and R. L. Borup, *J. Electrochem. Soc.*, **165**, F3166 (2018).
29. C. Takei, K. Kakinuma, K. Kawashima, K. Tashiro, M. Watanabe, and M. Uchida, *J. Power Sources*, **324**, 729 (2016).
30. W. Bi, Q. Sun, Y. Deng, and T. F. Fuller, *Electrochim. Acta*, **54**, 1826 (2009).
31. M. Uchimura and S. S. Kocha, *ECS Trans.*, **11**, 1215 (2007).
32. Y. Liu, M. Murphy, D. Baker, W. Gu, C. Ji, J. Jorne, and H. A. Gasteiger, *ECS Trans.*, **11**, 473 (2007).
33. C. Simon, F. Hasche, D. Muller, and H. A. Gasteiger, *ECS Trans.*, **69**, 1293 (2015).
34. C. Simon, F. Hasché, and H. A. Gasteiger, *J. Electrochem. Soc.*, **164**, F591 (2017).
35. G. S. Harzer, A. Orfanidi, H. El-Sayed, P. Madkikar, and H. A. Gasteiger, *J. Electrochem. Soc.*, **165**, F770 (2018).
36. Y. Liu, M. W. Murphy, D. R. Baker, W. Gu, C. Ji, J. Jorne, and H. A. Gasteiger, *J. Electrochem. Soc.*, **156**, B970 (2009).
37. R. Makharia, M. F. Mathias, and D. R. Baker, *J. Electrochem. Soc.*, **152**, A970 (2005).
38. M. Eikerling and A. A. Kornyshev, *J. Electroanal. Chem.*, **475**, 107 (1999).
39. K. C. Neyerlin, W. Gu, J. Jorne, A. Clark, and H. A. Gasteiger, *J. Electrochem. Soc.*, **154**, B279 (2007).
40. K. C. Neyerlin, W. Gu, J. Jorne, and H. A. Gasteiger, *J. Electrochem. Soc.*, **154**, B631 (2007).
41. D. R. Baker, D. A. Caulk, K. C. Neyerlin, and M. W. Murphy, *J. Electrochem. Soc.*, **156**, B991 (2009).
42. R. K. Ahluwalia, X. Wang, J.-K. Peng, V. Konduru, S. Arisetty, N. Ramaswamy, and S. Kumaraguru, *J. Electrochem. Soc.*, **168**, 044518 (2021).
43. K. H. Kangasniemi, D. A. Condit, and T. D. Jarvi, *J. Electrochem. Soc.,*, **151**, E125 (2004).
44. R. N. Carter, S. S. Kocha, F. Wagner, M. Fay, and H. A. Gasteiger, *ECS Trans.*, **11**, 403 (2019).
45. T. R. Garrick, T. E. Moylan, M. K. Carpenter, and A. Kongkanand, *J. Electrochem. Soc.*, **164**, F55 (2016).
46. K. Shinozaki, H. Yamada, and Y. Morimoto, *J. Electrochem. Soc.*, **158**, B467 (2011).
47. B. M. Stühmeier, M. R. Pietsch, J. N. Schwämmlein, and H. A. Gasteiger, *J. Electrochem. Soc.*, **168**, 064516 (2021).
48. T. A. Greszler, D. Caulk, and P. Sinha, *J. Electrochem. Soc.*, **159**, F831 (2012).
49. R. M. Darling and J. P. Meyers, *J. Electrochem. Soc.*, **150**, A1523 (2003).
50. Y. Shao-Horn, W. C. Sheng, S. Chen, P. J. Ferreira, E. F. Holby, and D. Morgan, *Top. Catal.*, **46**, 285 (2007).
51. M. K. Debe, A. K. Schmoeckel, G. D. Vernstrom, and R. Atanasoski, *J. Power Sources*, **161**, 1002 (2006).
52. W. Bi and T. F. Fuller, *J. Electrochem. Soc.*, **155**, B215 (2008).
53. W. Bi and T. F. Fuller, *J. Power Sources*, **178**, 188 (2008).
54. J. Zhang, B. A. Litteer, W. Gu, H. Liu, and H. A. Gasteiger, *J. Electrochem. Soc.*, **154**, B1006 (2007).
55. S. Kawahara, S. Mitsushima, K.-I. Ota, and N. Kamiya, *ECS Trans.*, **3**, 7 (2006).
56. D. C. Johnson, D. T. Napp, and S. Bruckenstein, *Electrochim. Acta*, **15**, 1493 (1970).
57. K. Ehelebe, D. Escalera-López, and S. Cherevko, *Curr. Opin. Electrochem.*, **29**, 100832 (2021).
58. R. M. Darling and J. P. Meyers, *J. Electrochem. Soc.,*, **152**, A242 (2005).
59. K. Ehelebe, J. Knöppel, M. Bierling, B. Mayerhöfer, T. Böhm, N. Kulyk, S. Thiele, K. J. J. Mayrhofer, and S. Cherevko, *Angew. Chem. Int. Ed.,*, **60**, 8882 (2021).
60. M. S. Kang and Y. I. Joe, *J. Power Sources*, **77**, 49 (1999).
61. F. Coms, H. Xu, T. McCallum, and C. Mittelsteadt, *ECS Trans.*, **50**, 907 (2013).
62. H. A. Gasteiger, J. E. Panels, and S. G. Yan, *J. Power Sources*, **127**, 162 (2004).
63. H. A. Gasteiger, S. S. Kocha, B. Sompalli, and F. T. Wagner, *Appl. Catal., B*, **56**, 9 (2005).
64. K. Kinoshita, *J. Electrochem. Soc.*, **137**, 845 (1990).
65. F. Du et al., *J. Electrochem. Soc.*, **167**, 144513 (2020).
66. A. Orfanidi, P. Madkikar, H. A. El-Sayed, G. S. Harzer, T. Kratky, and H. A. Gasteiger, *J. Electrochem. Soc.,*, **164**, F418 (2017).
67. K. C. Neyerlin, W. Gu, J. Jorne, and H. A. Gasteiger, *J. Electrochem. Soc.*, **153**, A1955 (2006).
68. N. P. Subramanian, T. Greszler, J. Zhang, W. Gu, and R. R. Makharia, *ECS Trans.*, **41**, 985 (2011).
69. Y. Ono, T. Mashio, S. Takaichi, A. Ohma, H. Kanesaka, and K. Shinohara, *ECS Trans.*, **28**, 69 (2010).
70. T. V. Reshetenko and J. St-Pierre, *J. Electrochem. Soc.*, **161**, F1089 (2014).
71. S. Shukla, D. Stanier, M. S. Saha, J. Stumper, and M. Secanell, *J. Electrochem. Soc.*, **163**, F677 (2016).
72. K. Kudo, T. Suzuki, and Y. Morimoto, *ECS Trans.*, **33**, 1495 (2010).
73. N. Nonoyama, S. Okazaki, A. Z. Weber, Y. Ikogi, and T. Yoshida, *J. Electrochem. Soc.*, **158**, B416 (2011).
74. N. P. Subramanian, T. A. Greszler, J. Zhang, W. Gu, and R. Makharia, *J. Electrochem. Soc.*, **159**, B531 (2012).
75. J. X. Wang, F. A. Uribe, T. E. Springer, J. Zhang, and R. R. Adzic, *Faraday Discuss.*, **140**, 347 (2008).
76. T. Lazaridis and H. A. Gasteiger, *J. Electrochem. Soc.*, **168**, 114517 (2021).
77. K. J. J. Mayrhofer, D. Strmcnik, B. B. Blizanac, V. Stamenkovic, M. Arenz, and N. M. Markovic, *Electrochim. Acta,*, **53**, 3181 (2008).
78. M. Inaba, H. Yamada, J. Tokunaga, and A. Tasaka, *Electrochem. Solid-State Lett.*, **7**, A474 (2004).
79. K. Ono, K. Sekizawa, N. Takeuchi, T. Yoshida, and M. Sudoh, *ECS Trans.*, **50**, 33 (2013).
80. D. A. Caulk and D. R. Baker, *J. Electrochem. Soc.*, **157**, B1237 (2010).
81. T. Schuler, A. Chowdhury, A. T. Freiberg, B. Sneed, F. B. Spingler, M. C. Tucker, K. L. More, C. J. Radke, and A. Z. Weber, *J. Electrochem. Soc.*, **166**, F3020 (2019).
82. R. Petrone, D. Hissel, M. C. Péra, D. Chamagne, and R. Gouriveau, *Int. J. Hydrog. Energy*, **40**, 12489 (2015).
83. S. Jomori, K. Komatsubara, N. Nonoyama, M. Kato, and T. Yoshida, *J. Electrochem. Soc.*, **160**, F1067 (2013).
84. J. P. Meyers and R. M. Darling, *J. Electrochem. Soc.*, **153**, A1432 (2006).
85. P. T. Yu, W. Gu, R. Makharia, F. T. Wagner, and H. A. Gasteiger, *ECS Trans.*, **3**, 797 (2006).
86. A. Collier, H. Wang, X. Zi Yuan, J. Zhang, and D. P. Wilkinson, *Int. J. Hydrogen Energy*, **31**, 1838 (2006).